The relative abundances of resolved $^{12}CH_2D_2$ and $^{13}CH_3D$ and mechanisms controlling isotopic bond ordering in abiotic and biotic methane gases

E. D. Young[*1], I. E. Kohl[1], B. Sherwood Lollar[2], G. Etiope[3], D. Rumble III[4], S. Li (李姝宁)[1], M. A. Haghnegahdar[1], E. A. Schauble[1], K. A. McCain[1], D. I. Foustoukos[4], C. Sutclife[2], O. Warr[2], C. J. Ballentine[5], T.C. Onstott[6], H. Hosgormez[7], A. Neubeck[8], J. M. Marques[9], I. Pérez-Rodríguez[10], A. R. Rowe[10], D. E. LaRowe[10], C. Magnabosco[11], Laurence Y. Yeung[12], Jeanine L. Ash[1],and L. T. Bryndzia[13]

Abstract

We report measurements of resolved $^{12}CH_2D_2$ and $^{13}CH_3D$ at natural abundances in a variety of methane gases produced naturally and in the laboratory. The ability to resolve $^{12}CH_2D_2$ from $^{13}CH_3D$ provides unprecedented insights into the origin and evolution of CH_4. The results identify conditions under which either isotopic bond order disequilibrium or equilibrium are expected. Where equilibrium obtains, concordant $\Delta^{12}CH_2D_2$ and $\Delta^{13}CH_3D$ temperatures can be used reliably for thermometry. We find that concordant temperatures do not always match previous hypotheses based on indirect estimates of temperature of formation nor temperatures derived from CH_4/H_2 D/H exchange, underscoring the importance of reliable thermometry based on the CH_4 molecules themselves. Where $\Delta^{12}CH_2D_2$ and $\Delta^{13}CH_3D$ values are inconsistent with thermodynamic equilibrium, temperatures of formation derived from these species are spurious. In such situations, while formation temperatures are unavailable, disequilibrium isotopologue ratios nonetheless provide novel information about the formation mechanism of the gas and the presence or absence of multiple sources or sinks. In particular, disequilibrium isotopologue ratios may provide the means for differentiating between methane produced by abiotic synthesis versus biological processes. Deficits in $^{12}CH_2D_2$ compared with equilibrium values in CH_4 gas made by surface-catalyzed abiotic reactions are so large as to point towards a quantum tunneling origin. Tunneling also accounts for the more moderate depletions in $^{13}CH_3D$ that accompany the low $^{12}CH_2D_2$ abundances produced by abiotic reactions. The tunneling signature may prove to be an important tracer of abiotic methane formation, especially where it is preserved by dissolution of gas in cool hydrothermal systems (e.g., Mars). Isotopologue signatures of abiotic methane production can be erased by infiltration of microbial communities, and $\Delta^{12}CH_2D_2$ values are a key tracer of microbial recycling.

1. Introduction

Measurements of multiply-substituted $^{13}CH_3D$ species in CH_4 gas have been used recently to estimate temperatures of formation of natural gases, identify gases of microbial origin that exhibit departures from isotopic bond-order equilibrium, and to elucidate mixing between thermogenic and biogenic methane (Ono et al. 2014; Stolper et al. 2014; Stolper et al. 2014; Stolper et al. 2015; Wang et al. 2015). Beginning in 2008, we embarked on a project to develop and employ a prototype mass spectrometer that is capable of resolving the two mass-18 isotopologues of methane, $^{12}CH_2D_2$ and $^{13}CH_3D$, for high-precision isotope ratio analysis (Young et al. 2016). Here we report measurements of resolved $^{12}CH_2D_2$ and $^{13}CH_3D$ at natural abundances made using this instrument. Samples include a variety of methane gases produced naturally and in the laboratory. The use of two multiply-substituted isotopic species provides insights into the provenance of methane gases, the physical chemical pathways of methane formation, and subsequent processing.

Reasons for studying the isotopic compositions of methane molecules are far ranging. The origins of natural gases, a major source of energy for the near future, serves as an important example. Another is the highly uncertain global atmospheric budget of methane, a key greenhouse gas. Yet another is the discovery of methane in the atmosphere of Mars as well as methane emanations from martian meteorites (Blamey et al. 2015; Webster et al. 2015). Indeed, methane and other alkanes are prevalent in outer solar system bodies (e.g., Brown et al. 2008), and there is the need to identify formation pathways of methane gas throughout the solar system. In extra-terrestrial applications, isotopic bond ordering can be particularly useful where our understanding of the bulk isotope ratios of various relevant reservoirs is poor to nonexistent.

One of the most pressing issues concerning the provenance of CH_4 gases is the need for reliable signatures of abiotic vs. biotic sources (Sherwood Lollar et al. 2006; Etiope and Sherwood Lollar 2013). The major sources of methane in commercial natural gas fields are biotic,

66 coming either from thermal cracking of sedimentary organic material (primary thermogenic) or
67 oil (secondary thermogenic), or from microbial methanogenesis (microbialgenic or "biogenic")
68 (e.g., Schoell 1988). Abiotic methane is produced in abundance in some geological settings such
69 as marine hydrothermal vents (Kelley et al. 2005; Proskurowski et al. 2008), in continental
70 ultramafic terranes exposed to fluids leading to serpentinization (Horita and Berndt 1999; Etiope
71 and Sherwood Lollar 2013; Schrenk et al. 2013) and in terrestrial Precambrian crust related to H_2
72 production from both serpentinization and radiolysis of water (Sherwood Lollar et al. 2002;
73 Sherwood Lollar et al. 2014). While comprising globally significant sources of methane, these
74 abiotic sources are generally regarded as being of little commercial significance due to the
75 ephemeral and unpredictable nature of their reservoirs deep in fractured crystalline rocks
76 (Sherwood Lollar et al. 2002; Glasby 2006). Nonetheless, the origin of gas in the world's second
77 largest gas field, Urengoy in Western Siberia, has been attributed variously to bacterial methane
78 generation, thermal breakdown of deeply buried mature organic matter, and abiotic
79 thermocatalytic reduction of CO_2 (Cramer et al. 1998 and references therein).

80 The typical isotopic tracers of methane provenance are $^{13}C/^{12}C$ (reported as $\delta^{13}C$[1] relative to
81 VPDB) and D/H (reported as δD relative to VSMOW). While isotope ratios of carbon and
82 hydrogen have proved useful for tracing the origins of natural methane (Schoell 1988; Etiope and
83 Sherwood Lollar 2013), these ratios by themselves can be ambiguous; there is overlap between
84 some empirically derived ranges defined by these isotope ratios for different sources of methane.
85 For example, the carbon isotope ratios associated with thermogenic methane formation and
86 microbial activity, partially overlap with those for abiotic methane formation (Horita and Berndt
87 1999; Tang et al. 2000; Cramer 2004).

[1] Throughout this paper we make use of the convention dating back to McKinney et al. (1950) that delta symbols refer to per mil deviations of an isotope ratio from a standard. All small and capital delta symbols in this work have units of per mil.

88 The ambiguity is exacerbated by the fact that in many geological settings methane sources are
89 likely to be mixed (Etiope and Sherwood Lollar 2013). A mixture of thermogenic and
90 microbialgenic gas is difficult if not impossible to identify using just bulk $\delta^{13}C$ and δD, but
91 should be identifiable using isotopic bond ordering (e.g., Young et al. 2011; Stolper et al. 2015;
92 Young et al. 2016). Other geochemical signatures of methane formation pathways can help
93 disambiguate the conclusions based on bulk isotope ratios alone. For example, a decrease in $\delta^{13}C$
94 with increasing carbon number for gaseous n-alkanes (C1-C4) can be a line of evidence for
95 abiotic formation, while a strongly positive relationship between $\delta^{13}C$ and carbon number reflects
96 a thermogenic origin (Sherwood Lollar et al. 2002; McCollom and Seewald 2007). However, the
97 $^{13}C/^{12}C$ composition of hydrocarbons experimentally formed during Fischer-Tropsch-Type (FTT)
98 synthesis under hydrothermal conditions (McCollom and Seewald 2006; Fu et al. 2007) and
99 measured in the alkaline vent fluids of Lost City (Proskurowski et al. 2008) appear to deviate
100 from the "abiotic" trends referred to above. This suggests that the magnitude of fractionations and
101 isotopic trends among light alkanes are likely affected by mineral-catalyst composition and the
102 kinetic rates of FTT reactions (Sherwood Lollar et al. 2008). By characterizing the bond ordering
103 of ^{13}C and D in CH_4, the role of methane formation mechanism on the C-H bond can be assessed
104 in the absence of subsequent polymerization reactions. It is evident, therefore, that an ideal and
105 robust tracer for methane formation mechanisms would be one based on the methane molecule
106 itself.

107 The initial motivation for the development of methane isotopologue tracers was the utility of
108 $^{13}CH_3D/^{12}CH_4$ ratios as formation temperature indicators. Intermolecular isotope exchange
109 thermometers like D/H exchange between CH_4 and H_2 gas rely on the assumption of exchange
110 equilibrium. An intra-species thermometer would be more robust. Methane sources that can be
111 distinguished on the basis of temperature include microbial production in sedimentary source
112 rocks with an upper temperature limit of ~ 70 to 90°C and higher-temperature thermogenic

methane production that often occurs at > 140°C, or abiotic methane produced in high-temperature hydrothermal systems at > 300°C. However, temperature alone will not be entirely diagnostic. Thermogenic methane can be produced at temperatures as low as 60 to 70°C (diagenesis or low-T catagenesis), overlapping the range for microbial methanogenesis. Serpentinization, a source of hydrogen to produce methane, occurs at temperatures at least as low as 50°C (Schrenk et al. 2013 and references therein), and so abiotic methane production also overlaps with microbial methanogenesis in temperature (Etiope and Sherwood Lollar 2013 and references therein). Overlap occurs at high temperatures between thermogenic gas from biotic sources and abiogenic processes like high-temperature oxidation-reduction in the deep crust or mantle (e.g., higher-*T* serpentinization) and catalyzed abiotic hydrocarbon production by FTT reactions (Horita and Berndt 1999; Foustoukos and Seyfried 2004; Etiope and Ionescu 2015). In addition, it is difficult to verify that a temperature derived from a measurement of $^{13}CH_3D/CH_4$ alone is valid; assessment of the degree of internal (intra-species) thermodynamic equilibrium is necessary to verify that a temperature obtained by isotopic bond ordering is valid.

Rather than relying on temperature estimates alone, the long-term goal should be to characterize the effects of various reactions and transport mechanisms on the distributions of rare isotopologues. The goal of this study is to investigate the advantages of using the relative concentrations of $^{12}CH_2D_2$ and $^{13}CH_3D$ to elucidate the origin of methane gas from a wide variety of geochemical settings. In particular, we set out to characterize methane produced abiotically, generally by surface catalysis, and to compare those gases to those produced by microbial methanogenesis and to those originating from thermogenesis. We do this by analyzing samples produced in the laboratory and samples representing various natural sources of methane gas.

2. Fundamentals of $\Delta^{12}CH_2D_2$ vs. $\Delta^{13}CH_3D$ Space

2.1 Temperature

The concept of isotope bond ordering, or "clumping" as it has become known in the geosciences, is understood relative to the null condition of the purely stochastic distribution of isotopic species (isotopologues) of a molecule. In the case of methane one is concerned with the fraction of carbon that is the heavy isotope, ^{13}C:

$$X(^{13}\mathrm{C}) = \frac{^{13}\mathrm{C}}{^{13}\mathrm{C} + ^{12}\mathrm{C}} \tag{1}$$

and the fraction of the hydrogen isotopes that is deuterium, D:

$$X(\mathrm{D}) = \frac{\mathrm{D}}{\mathrm{H} + \mathrm{D}} \quad . \tag{2}$$

The random distribution of isotopologues is then derived by treating these fractional abundances as probabilities such that, for example

$$\begin{aligned} X(^{12}\mathrm{CH_4}) &= X(^{12}\mathrm{C})(X(\mathrm{H}))^4 \\ X(^{13}\mathrm{CH_4}) &= X(^{13}\mathrm{C})(X(\mathrm{H}))^4 \\ X(^{12}\mathrm{CH_3D}) &= 4X(^{12}\mathrm{C})(X(\mathrm{H}))^3 X(\mathrm{D}) \\ &\vdots \end{aligned} \tag{3}$$

where multiplicity from isotopomer (isotopic isomer) abundances are accounted for by exponents in Equation (3). Exchange of isotopes between isotopologues occurs by reactions such as

$$^{13}\mathrm{CH_4} + ^{12}\mathrm{CH_3D} \rightleftharpoons ^{12}\mathrm{CH_4} + ^{13}\mathrm{CH_3D} \quad . \tag{4}$$

The equilibrium constant for this reaction is

$$K_{\mathrm{Eq},^{13}\mathrm{CD}} = \frac{\left[^{13}\mathrm{CH_3D}\right]\left[^{12}\mathrm{CH_4}\right]}{\left[^{13}\mathrm{CH_4}\right]\left[^{12}\mathrm{CH_3D}\right]} \tag{5}$$

where the square brackets denote concentrations that can be equated with the fractional abundances like those in Equations (3). At high temperatures (≥ 1000 K) the distributions of isotopologues is effectively random (stochastic) and substitution of the fractional abundances in Equations (3) into the equilibrium constant in Equation (5) yields

156 $$K_{\mathrm{Eq},^{13}\mathrm{CD},\,\mathrm{stoch}} = \frac{\left[{}^{13}\mathrm{CH_3D}\right]\left[{}^{12}\mathrm{CH_4}\right]}{\left[{}^{13}\mathrm{CH_4}\right]\left[{}^{12}\mathrm{CH_3D}\right]} = \frac{4X({}^{13}\mathrm{C})(X(\mathrm{H}))^3 X(\mathrm{D}) X({}^{12}\mathrm{C})(X(\mathrm{H}))^4}{4X({}^{12}\mathrm{C})(X(\mathrm{H}))^3 X(\mathrm{D}) X({}^{13}\mathrm{C})(X(\mathrm{H}))^4} = 1\ . \quad (6)$$

157 An equilibrium constant of unity in this case corresponds to a purely random distribution of
158 isotopes among the molecules. At lower temperatures the stabilizing effects of two heavy
159 isotopes bonded together begins to take hold and the equilibrium constant in Equation (5) gets
160 progressively larger as *T* goes down. This enhancement in rare multiply-substituted
161 isotopologues, or clumping, is expressed in delta notation as

162 $$\Delta_{^{13}\mathrm{CH_3D}} = 10^3\left(\frac{X_{^{13}\mathrm{CH_3D}}}{X_{^{13}\mathrm{CH_3D},\,\mathrm{Stochastic}}} - 1\right). \quad (7)$$

163 Similarly, internal isotope exchange leading to doubly-deuterated methane can be described by
164 the reaction

165 $$2\,{}^{12}\mathrm{CH_3D} \rightleftarrows {}^{12}\mathrm{CH_2D_2} + {}^{12}\mathrm{CH_4} \quad (8)$$

166 with the equilibrium constant

167 $$K_{\mathrm{Eq},\mathrm{CH_2D_2}} = \frac{\left[{}^{12}\mathrm{CH_2D_2}\right]\left[{}^{12}\mathrm{CH_4}\right]}{\left[{}^{12}\mathrm{CH_3D}\right]^2} \quad (9)$$

168 The stochastic value for the equilibrium constant for reaction (8) is

169 $$K_{\mathrm{Eq},\mathrm{CH_2D_2},\,\mathrm{stoch}} = \frac{\left[{}^{12}\mathrm{CH_2D_2}\right]\left[{}^{12}\mathrm{CH_4}\right]}{\left[{}^{12}\mathrm{CH_3D}\right]^2} = \frac{6X({}^{12}\mathrm{C})(X(\mathrm{H}))^2(X(\mathrm{D}))^2 X({}^{12}\mathrm{C})(X(\mathrm{H}))^4}{[4(X(\mathrm{H}))^3 X(\mathrm{D})\ X({}^{12}\mathrm{C})]^2} = \frac{6}{16} \quad (10)$$

170 such that a stochastic distribution of isotopes leads to an equilibrium constant of 3/8. Per mil
171 departures from this stochastic ratio are quantified using

172 $$\Delta_{^{12}\mathrm{CH_2D_2}} = 10^3\left(\frac{X_{^{12}\mathrm{CH_2D_2}}}{X_{^{12}\mathrm{CH_2D_2},\,\mathrm{Stochastic}}} - 1\right). \quad (11)$$

The two parameters $\Delta^{12}CH_2D_2$ and $\Delta^{13}CH_3D$ can serve as independent intra-molecular thermometers where thermodynamic equilibrium obtains. The relationships between temperature and both $\Delta^{12}CH_2D_2$ and $\Delta^{13}CH_3D$ are calculable (e.g., Ma et al. 2008; Webb and Miller 2014; Liu and Liu 2016) and the loci of thermodynamic equilibrium in a plot of $\Delta^{12}CH_2D_2$ vs. $\Delta^{13}CH_3D$ serves as a useful reference (Figure 1). *Ab initio* calculations by one of us (EAS) for equilibrium constants yield these expressions used to define the equilibrium curve in $\Delta^{12}CH_2D_2$ vs. $\Delta^{13}CH_3D$ space:

$$K_{EQ,\ ^{13}CD} = 1 + 0.0355502/T - 433.038/T^2 + 1270210.0/T^3 - 5.94804\times10^8/T^4 + 1.196630\times10^{11}/T^5 - 9.07230\times10^{12}/T^6 \quad (12)$$

$$(8/3)K_{EQ,CH_2D_2} = 1 + 0.183798/T - 785.483/T^2 + 1056280.0/T^3 + 9.37307\times10^7/T^4 - 8.919480\times10^{10}/T^5 + 9.901730\times10^{12}/T^6 \quad (13)$$

where T is in K. Differences in the theoretical $\Delta^{13}CH_3D$ vs. temperature relationships due to different computational methods are less than the current analytical uncertainties in the measurements for methane (Webb and Miller 2014; Liu and Liu 2016) and the same is most likely true for $\Delta^{12}CH_2D_2$.

2.2 Departures from Equilibrium

Departures from equilibrium as represented by $\Delta^{12}CH_2D_2$ and $\Delta^{13}CH_3D$ can arise from bond rupture and bond formation limited by kinetics, but can also arise from any process that alters the bulk isotopic composition of the gas. This is because the stochastic ratios comprising the denominators in Equations (7) and (11) are calculated from the bulk isotopic compositions, and if these bulk compositions do not represent the values that obtained during bond formation, the shift in reference frame leads to departures from the curve in Figure 1. One mechanism for departures from the equilibrium curve is therefore mixing of two gases (Eiler and Schauble 2004). In the case of methane, two CH_4 gases with different bulk $^{13}C/^{12}C$ and/or D/H result in clear departures

195 from equilibrium (Young et al. 2016). Figure 2 shows the effects of mixing as measured in our
196 laboratory (Young et al. 2016). For many naturally-occurring isotope ratios, mixing results in
197 positive excursions from equilibrium. This property of $\Delta^{12}CH_2D_2$ vs. $\Delta^{13}CH_3D$ space alone is a
198 novel and important new tracer because in many natural methane occurrences mixing of distinct
199 sources (e.g., microbial, thermogenic, abiotic) may have led to inconsistencies in interpretations
200 (Etiope and Sherwood Lollar 2013).

201 Kinetics and diffusion are two additional ways to produce deviations from equilibrium
202 $\Delta^{12}CH_2D_2$ and $\Delta^{13}CH_3D$ values. We have modeled molecular diffusion of CH_4 through an orifice
203 (representing a permeable medium) as a Rayleigh process using Graham's law. Because the
204 slope of molecular diffusion in $\Delta^{12}CH_2D_2$ vs. $\Delta^{13}CH_3D$ space is nearly unity (because both axes
205 refer to ~18/16 molecular mass ratios), while the slope of the equilibrium curve is greater,
206 diffusion results in residues with positive displacements in $\Delta^{12}CH_2D_2$ relative to the equilibrium
207 curve (Figure 3). The greater the diffusive loss, the greater the apparent excess in $^{12}CH_2D_2$ in the
208 residual gas relative to equilibrium. Diffused gas behaves similarly but starts out to the right of
209 the equilibrium curve and evolves to the left in Figure 3. *Ab initio* calculations depicting the
210 kinetics of CH_4 destruction by reaction with the OH radical in the atmosphere (Haghnegahdar et
211 al. 2015) produce a different trajectory in $\Delta^{13}CH_3D - \Delta CH_2D_2$ space with negative displacements
212 in the latter (Figure 3). In both cases, the ability to measure both $\Delta^{13}CH_3D$ and $\Delta^{12}CH_2D_2$ is
213 crucial for identifying methane affected by these processes.

214 **3. Samples and Methods**

215 We report bulk isotopic and isotopologue ratio measurements of methane gases collected from
216 across the globe in a variety of settings, with an emphasis on instances where a significant abiotic
217 component has been reported in previous work. We also present measurements of gases
218 produced in the laboratory by abiotic processes and by microbial methanogenesis. The goal is to
219 use the laboratory experiments as guides for interpreting the results from natural samples, all the

while being cognizant of the fact that laboratory conditions cannot mimic the natural conditions perfectly.

3.1 Natural samples

A pressing problem in determining the provenance of methane gas is distinguishing reliably biotic (microbial production or thermal decomposition of existing organic matter) from abiotic sources. We have therefore sampled sources of putative abiotic CH_4 gas across the globe together with thermogenic gases and gases thought to have a significant microbialgenic component.

Continent-bound ultramafic igneous complexes: We measured methane gases from three continent-bound ultramafic igneous complexes comprising two obducted ophiolite sequences and a peridotite intrusion. On-shore ultramafic igneous rock terranes such as these have been recognized relatively recently as important sources of abiotic CH_4 (Etiope and Sherwood Lollar 2013). The largest of these is the Chimaera seep, or "flaming rock" from southwestern Turkey (Figure 4). Known since antiquity, here methane gas emanates through surface vents from fractures in a 5000 m^2 outcrop of the Upper Cretaceous Tekirova ophiolite (Etiope et al. 2011). Low-temperature abiotic methane generation is thought to be catalyzed by rhuthenium in the host rock (Etiope and Ionescu 2015). Temperatures of formation have been estimated to be < 100^{o}C, and perhaps ~ 50^{o}C based on the D/H distribution between CH_4 and H_2 and the assumption of inter-species isotopic equilibrium (Etiope et al. 2011). The carbon source for the methane has been dated to be > 50,000 years old based on the absence of ^{14}C (Etiope and Schoell 2014).

A methane sample from another on-shore igneous complex was collected from a borehole at the Cabeço de Vide mineral water spa, Portugal. Here methane is dissolved in hyperalkaline (pH > 11) waters issuing from natural springs and boreholes drilled in the Alter-do-Chão mafic-ultramafic massif of Ordovician age (Etiope et al. 2013). Serpentinites are distributed to a depth of about 1 km and serpentinization is driven by meteoric water recharge from the surface. At a maximum depth of 1 km and with a temperature gradient of ~30^{o}C/km, temperatures of formation

245 are thought to be less than 100°C. Spring waters have a temperature of 20°C. The exact timing of
246 CH_4 production is uncertain because the role of ongoing reactions versus storage of older gas is
247 unresolved (Etiope et al. 2013).

248 We also measured a sample from the Acquasanta Terme hyperalkaline spring waters issuing
249 from serpentinized ophiolites from the north of Italy (Figure 4) (Boschetti et al. 2013). Here
250 again meteoric waters recharge the system and drive reactions with the ultramafic complex to
251 produce methane at what are believed to be temperatures of < 100°C. Based on the assumption of
252 D/H equilibrium between H_2O and CH_4, Boschetti et al. estimate a temperature of CH_4 formation
253 of ~ 60°C. Methane is free of ^{14}C, indicating that the carbon source is > 50,000 years old
254 (Whiticar and Etiope 2014).

255 *Precambrian cratons*: Precambrian cratons account for > 70% of the continental lithosphere
256 and are now recognized as major contributors to the global budget of H_2 (Sherwood Lollar et al.
257 2014) that can produce CH_4 from various crustal sources of carbon. The sources of H_2 are
258 thought to be radiolysis of water and/or water-rock reactions at great depth (Sherwood Lollar et al.
259 2014). Production of CH_4 can occur by abiotic organic synthesis or by microbial methanogenesis
260 where microbial communities are extant in the deep subsurface (Sherwood Lollar et al. 2002;
261 Ward et al. 2004; Lin et al. 2006; Sherwood Lollar et al. 2006; Sherwood Lollar et al. 2008). We
262 analyzed deep mine samples from the Witwatersrand Basin, South Africa and from the Canadian
263 Shield. Sites were selected to represent those with ostensible abiotic CH_4 production, those with a
264 microbial CH_4 source, and also those thought to contain mixtures of the two sources. Sampling
265 methods are similar to those described by Ward et al. (2004).

266 We analyzed gases from four ultra-deep gold mines from the Witwatersrand Basin, including
267 the Beatrix, Masimong, Kloof, and Tau Tona mines (Figure 4). Sampling depths were from ~1
268 km (Beatrix) to 3.3 km (Kloof). The Witwatersrand lies within the Archean Kaapvaal Craton and
269 is composed of 2900 to 2500 Ma volcanosedimentary sequences of various lithologies overlying

3450 Ma granite-greenstone and the 3074 Ma volcanosedimentary rocks (Ward et al. 2004). A meteorite impact 2 Gyr before present modified the structure in the central part of the Basin.

Studies from mines throughout the craton have demonstrated the presence of saline aqueous fluids occupying interconnected fractures in the crystalline rocks. The fracture waters from the Witwatersrand Basin are composed of varying proportions of two endmembers consisting of shallower, less saline paleo-meteoric waters and deeper, older, and more saline waters (Onstott et al. 2003; Ward et al. 2004). These paleo-meteoric fracture waters have residence times that range from tens of thousands (Borgonie et al. 2015) to several millions of years (Lippmann et al. 2003). They have negligible dissolved H_2 and are thought to contain CH_4 largely of microbial origin (Ward et al. 2004; Sherwood Lollar et al. 2008). The deeper, more saline fracture waters have high concentrations of dissolved H_2 and are thought to contain abiotic CH_4. They have residence times of tens of millions of years (Lippmann et al. 2003; Lippmann-Pipke et al. 2011).

Waters from the Beatrix, Masimong, and Tau Tona mines are dominated by the paleo-meteoric component. Beatrix waters have estimated residence times of ~3 to 5 million years based on noble gas isotope ratios (Lippmann et al. 2003). Residence times for waters in the Masimong mine can be inferred from noble gas analyses from other mines in the same mining camp and are 1 to 129 million years (Lippmann et al. 2003). The estimated residence time for the Tau Tona waters is less than 10 million years. In contrast to the other three localities, the Kloof mine waters have isotopic characteristics suggesting the presence of the older, more evolved fluid component. Residence times for the Kloof waters are on the order of 15-20 million years (Lippmann et al. 2003).

Present-day water temperatures in the Witwatersrand mines vary from ~30^{o}C for samples collected at depths of ~1 km to ~50^{o}C for the samples collected at ~3 km (Kieft et al. 2005; Simkus et al. 2016). Fission track ages from rocks of the Witwatersrand basin indicate that the maximum temperatures of ~ 100^{o}C existed within the meteoric water flow system ≤ ~ 65 Myr before present at paleo-depths of 5 to 6 km (Omar et al. 2003). Present-day temperatures at

296 depths of several km were established in these rocks by ~ 30 Myr BP. Local variations in
297 thermal gradients past and present resulted from groundwater advection (Omar et al. 2003).
298 Earlier studies showed several lines of evidence for a significant microbial component to the
299 CH_4 gas from the Beatrix and Masimong mines and archaea are documented at the Beatrix,
300 Masimong, and Tau Tona sites (Ward et al. 2004; Simkus et al. 2016). For the Beatrix and
301 Masimong sites, low $\delta^{13}C$, moderate δD, and relatively high C1/C2+ (i.e., $CH_4/(C_2H_6 + C_3H_8$
302 +…)) all point to dominantly microbial methane mixed with a minor non-microbial endmember
303 (Ward et al. 2004). In contrast, gases from the Kloof and Tau Tona mines may represent
304 mixtures between methane produced by subsurface microbial communities and abiotic methane
305 produced by water-rock reactions fed by mM concentrations of dissolved H_2 in the older, deeper
306 systems (Sherwood Lollar et al. 2006; Sherwood Lollar et al. 2008). Methane from both mines
307 exhibit higher $\delta^{13}C$ values and lower δD values, suggesting less of a microbial component at
308 these sites than at the Beatrix and Masimong mines. What is more, no evidence for methanogens
309 was found in Kloof mine samples (Kieft et al. 2005). In general, deeper, more saline and
310 chemically evolved waters in the mines are associated with low biodiversity chemoautotrophic
311 microbial communities isolated from the surface (Lin et al. 2006; Lippmann-Pipke et al. 2011),
312 suggesting that there might be an inverse correlation between the microbial component of CH_4
313 and the antiquity of the waters.
314 Methane gases from two mines from the Canadian Shield were analyzed in this study. As in
315 the case of the South African gold mines, methane from these localities is dissolved in saline
316 groundwaters isolated within fracture systems in the rocks. The two sites were selected for this
317 study because they appear to represent distinct methane end-members for these fracture fluid
318 systems, one dominantly microbial in origin and the other mainly abiotic in origin. Gas is
319 sampled upon depressurization into the mine through boreholes and seeps using methods
320 descrbied by Ward et al. (2004) and Sherwood Lollar et al. (2006).

321 The Kidd Creek mine is within one of the world's largest volcanogenic massive sulfide
322 deposits and, extending from the surface to a depth of 3km, it is also one of the world's deepest
323 working mines. It is located in the southern volcanic zone of the Abitibi greenstone belt (2700
324 Ma), north of Timmins Ontario, Canada (Figure 4). Kidd Creek is the most extensively studied
325 locality in our data set. Some sample sites at Kidd Creek have been monitored continuously for a
326 decade or more ever since an abiotic origin for methane in the mine at the 6800 foot level (2072
327 meters) was first proposed (Sherwood Lollar et al. 2002). Since that time, fluids have been
328 studied from all levels down to the current operating depth of 9800 feet (2987 meters). The
329 deepest, most saline fluids in the mine have billion year residence times deduced from dissolved
330 noble gases, some of which may be vestiges of Archean atmosphere (Holland et al. 2013).
331 Data are presented from samples collected at two levels in the mine (7850 and 9500 feet) and
332 collected over a period of 8 years. Measured water temperatures at depths corresponding to the
333 samples used here are about 23°C to 26°C at the 7850 level and 29°C to 32°C at the 9500 level
334 The Kidd Creek gas is considered to be an example of low-temperature abiotic methane in part by
335 virtue of its low bulk δD values, relatively high $\delta^{13}C$ values, low CH_4/C_2+, the $^{13}C/^{12}C$ ratios of
336 associated ethane, propane, and butane, and crustal, as opposed to mantle, $^{3}He/^{4}He$ (Sherwood
337 Lollar et al. 2006).
338 Birchtree is a nickel mine located in Manitoba, Canada and is part of the same property as the
339 Thompson mine. It lies within the Circum-Superior Belt igneous province (Figure 4). The sample
340 used in this study was sampled at a depth of 1200 meters. Water temperatures are 20°C to 22.5°C.
341 The sample was selected because the methane from this locality is thought to be largely the
342 product of microbial methanogenesis.
343 *Shale gas*: Nominally thermogenic gases are represented in this study by samples of the
344 Utica and Marcellus shales from the Appalachian Basin of the eastern United States (Figure 4).
345 The Marcellus Shale is a black carbonaceous shale of Middle Devonian age occurring at a
346 maximum depth of about 1.6 km beneath the states of Pennsylvania, New York and West

Virginia, United States, rising to shallower depths westward into the neighboring state of Ohio. The sample used in this study is from a Shell well from central Pennsylvania. The Utica Shale lies hundreds of meters to ~2 km beneath the Marcellus and comprises organic-rich calcareous black shale of Middle Ordovician age (Rowan 2006). The sample used here is also from central Pennsylvania. Methane exists in low-permeability pore space and in fractures (both units are unconventional economic gas sources). The gases are generally agreed to be thermogenic in origin (Jenden et al. 1993). Present-day temperature at the maximum depth of the Marcellus Shale is about 60^{o}C while at the maximum depth of the Utica Shale it is about 90^{o}C (Rowan 2006). Modeling of the thermal history of the Appalachian Basin in general suggests that the lower units experienced maximum temperatures of 250 to as high as 300^{o}C (Burruss and Laughrey 2010). Thermal modeling described briefly by Stolper et al. (2014) in a supplement suggests that the Marcellus Shale experienced maximum burial 270 Myr before present with maximum temperatures of ~ 180^{o}C and methane generation at 173^{o}C. The thermal histories of these rocks are complicated by burial metamorphism following Alleghanian thrust faulting. Burruss and Laughrey (2010) suggest that mixing of gases with disparate $^{13}C/^{12}C$ and D/H has occurred for Utica gases, perhaps resulting in reverse isotope effects in which $\delta^{13}C$ (CH_4) > $\delta^{13}C$ (C_2H_6) > $\delta^{13}C$ (C_3H_8) > $\delta^{13}C$ (C_4H_{10}). Minor extant microbial activity has been documented in the Marsellus wells in Pennsylvania, including low abundances of halo-tolerant methanogens (Cluff et al. 2014).

A sample from the Beecher Island gas field of the Denver Basin, Yuma County, Colorado (Figure 4) was provided to us by the U.S. Geological Survey for analysis. The gas derives from the Cretaceous Niobrara Formation at a depth of ~500 to 550 meters (Lockridge 1977). Although thermogenic gases are produced elsewhere in the Niobrara at greater depths, methane from this relatively shallow depths has been classified as “biogenic” (implying microbial) in origin (Lehr and Keeley 2016).

3.2 FTT synthesis of CH_4 at low temperatures

We analyzed gases produced by the Sabatier reaction:

$$CO_2 + 4H_2 \rightarrow CH_4 + 2H_2O \quad (14)$$

catalyzed by ruthenium (Ru) using methods described by Etiope and Ionescu (2015). These experiments are meant to simulate the production of methane at relatively low temperatures in serpentinized ultramafic rock environments. In brief the reaction proceeded in borosilicate glass Wheaton bottles filled with ~ 5 ml of CO_2 and 50 ml of H_2 diluted with Ar as a makeup gas. The metal catalyst was ~ 3 g of 3.8% Ru on alumina support (Ru mainly in the form of RuO_2 as it may occur in natural chromites). Bottles were held in a temperature-controlled oven at 70°C (up to 210 hours) and 90°C (for 30 days).

3.3 $Si_5C_{12}H_{36}$ decomposition experiments

A series of cold-seal experiments was conducted at the Geophysical Laboratory to constrain kinetic and equilibrium $\Delta^{12}CH_2D_2$ and $\Delta^{13}CH_3D$ effects of methane production at high temperatures (300 to 600°C) and pressures (100MPa) (Table 1). In these experiments $Si_5C_{12}H_{36}$ (tetrakis(trimethylsilyl) silane) reacts with H_2O to produce $SiO_{2(s)}$, CH_4 and H_2:

$$Si_5C_{12}H_{36} + 10H_2O \rightarrow 5SiO_2 + 12CH_4 + 4H_2 \ . \quad (15)$$

By this reaction CH_4 is produced by CH_3 escape from the silane structure followed by addition of hydrogen. The samples consisted of H_2O (~50 mg) and $Si_5C_{12}H_{36}$ (~3 mg, Alfa Aesar 98% - natural D/H abundance) along with a roughly 2 mg mixture of Ni (Alfa Aesar, Puratronic 99.996%, <10 μm diameter grain) and Pt metals (100 μm x 70μm OD rod) with no specific in-plane crystal orientation (e.g. Ni(111), Pt(111)). Reaction times were from 286 (600 °C) to 453 (300 – 500 °C) hours. Previous in-situ and real-time observations have shown that complete decomposition of $Si_5C_{12}H_{36}$ occurs within as little as 5 min at 600 °C (Foustoukos and Mysen 2013). In the current study, the experimentally produced CH_4 ranged from 104 to 194 μmole.

Reactants were placed in 2.5-cm long, 5-mm OD Au capsules. The Au tubes were annealed at 900 °C, boiled in 6 *N* nitric acid and finally cleaned with deionized water prior to use. The capsules were welded shut by a tungsten inert-gas high-frequency pulse welder that generates very low heat output, preventing H_2O volatilization (weight loss < 0.1 wt %). The experimental charges were hosted in ~30 ml pressure vessels (Tuttle 1949; Frantz et al. 1992) to minimize the quench times. Quenching was by immersion in a water bath. The average cooling rate is approximated to 100 °C/s between 600 °C and 100 °C. Immediately after cooling, capsules were weighed to check for leakage. Temperatures were recorded by sheathed chromel-alumel thermocouples placed in contact with the pressure medium (H_2O) (±1 °C). Pressure was monitored to ± 0.1 MPa by a Heise ST-2H digital gauge that is factory-calibrated.

Product gases were sealed in borosilicate breakseal tubes for shipment to UCLA. The breakseals were opened to the vacuum extraction system for isolation of CH_4.

3.4 Isotope exchange experiments

We used the intra-species exchange of isotopes for methane gas as a means of verifying the accuracy of our measurements. Methane gas was sealed in borosilicate or quartz breakseal tubes together with platinum on alumina. Breakseals were placed in a temperature-controlled tube furnace for 72 hours to a week. The breakseals were quenched in water or air and the gases released by cracking the glass directly into the purification vacuum line.

3.5 *Methanogens in the laboratory*

Isotope ratios for methane produced by three methanogen species and two substrates are reported here. The axenic cultures were grown at the University of Southern California in 100 to 160 ml crimped serum bottles. The carbon source is either 125 mM methanol or CO_2 dissolved in water. Conversion rate from methanol is ~ 75%. The data reported here include methane produced by *Methanosarcina barkeri* grown at 30°C by the reaction $4CH_3OH \rightarrow 3CH_4 + CO_2 + 2H_2O$,

420 *Methanosarcina acetivorans* at 30°C by the reaction $4CH_3OH \rightarrow 3CH_4 + CO_2 + 2H_2O$, and
421 *Methanothermococcus thermolithotrophicus* grown at 65°C by the reaction $HCO_3^- + 4H_2 + H^+ \rightarrow$
422 $CH_4 + 3H_2O$. CH_4 was extacted from the serum bottles using a gas-tight syringe and injected into
423 the vacuum line for purification.

424 *3.6 Microbial communities in Precambrian craton fracture waters*

425 In order to characterize the archaeal community composition in the fracture water from the
426 Beatrix, Masimong, and Tau Tona mine boreholes, the V6 hypervariable region of the archaeal
427 16S rRNA gene was amplified and sequenced as described in Simkus et al. (2016). A 100%
428 overlap quality filter was applied to the V6 paired end sequences and clustered using the
429 Minimum Entropy Decomposition (MED) pipeline (-A 0 –M 2 –d 4) (Eren et al. 2015).
430 Sequences that passed quality control and the MED pipeline were annotated using GAST (Huse
431 et al. 2008) and a GAST formatted V6 reference set (https://vamps.mbl.edu/ data_downloads/
432 refv6a.tgz).

433 *3.7 Gas purification*

434 We purify methane gas for isotopic analysis on a vacuum line interfaced with a gas
435 chromatograph (GC). Samples are delivered to the vacuum line through a septum by either gas-
436 tight syringe or with an 18 gauge needle attached to the line with a dedicated small-volume valve
437 (SGE SMOV). The vacuum line is composed of 316L tubing connected with VCR face seal
438 fittings (Swagelok) and Conflat CF flanges. It is hydrocarbon free, consisting of a
439 turbomolecular pump backed by a diaphragm rough pump. Sample gases are trapped on silica gel
440 at liquid-N_2 temperature. Helium carrier gas is then used to flush the sample gas from the silica
441 gel trap to the GC while warming the trap to ~ 30°C. Carbon dioxide is retained on silica gel at
442 room temperatures and is lost from the sample after warming the first trap. Purified methane
443 exiting the GC is trapped on a second silica gel trap at liquid-N_2 temperature for 30 minutes.

After slowly purging the trap of He the sample is transferred to an evacuated sample tube filled with silica gel. This tube is used to introduce the sample to the dual inlet of the mass spectrometer by expansion while heating the silica gel to 60^{o}C. Samples are mixed during expansion from the sample tube into the variable-volume bellows of the instrument for 20 to 40 minutes depending upon the size of the bellows used and the sample quantity. Mixing is promoted by squeezing and expanding the variable-volume bellows and by applying freeze/thaw cycles on the silica gel. Mixing ensures isotope fidelity when expanding from the sample tube to the variable volume of the instrument.

Two GC columns are used in series for purification. The first is a 3-meter 1/8 inch OD stainless steel (SS) column packed with 5A molecular sieve. This is followed by a 2-meter 1/8 inch OD SS column packed with HayeSep D porous polymer. Flow rate of the He carrier gas is 20 ml/min and the columns are held at a fixed temperature of 25^{o}C during sample processing. The first column separates H_2, Ar, O_2 and N_2 from methane and other hydrocarbons. The second column separates CH_4 from C_2H_6, C_3H_8 and higher order hydrocarbons. Peaks are identified using a passive TCD detector. Retention times of base-line resolved methane are ~ 17 +/–1 minutes under these conditions. Thirty-minute collection times ensure capture of all of the eluting methane peak tail with isotope fidelity.

3.8 Mass spectrometry

We measured ion currents of $^{12}CH_4^+$, $^{13}CH_4^+$, $^{12}CH_3D^+$, $^{13}CH_3D^+$ and $^{12}CH_2D_2^+$ for methane gas samples using the prototype Panorama (Nu Instruments) high-mass-resolution gas-source multiple collector mass spectrometer. Details surrounding the measurement of methane gas with this instrument were reported previously (Young et al. 2016). Here we summarize the measurement procedures. The reader is referred to Young et al. (2016) for a comprehensive description of the mass spectrometer and methods.

468 The instrument is set to a mass resolving power (MRP) of ~ 40,000 or greater (instrumental
469 $M/\Delta M$ where ΔM is defined at 5 and 10% peak heights) with an entrance slit width of ~ 35 µm.
470 At this resolution the two mass-18 rare isotopologues are effectively resolved (Figure 5). Mass
471 16 and mass 17 isotopologues are measured using Faraday collectors with amplifier resistors of
472 $10^{11}\Omega$. Both mass-18 isotopologues are measured with an electron multiplier as the axial
473 collector. Isotopologue ratios are obtained using two magnet current settings (Figure 5). In the
474 first setting, the magnet is set to place $^{13}CH_3D^+$ (mass = 18.04090 amu) in the axial collector and
475 ratios of $^{13}CH_4^+/^{12}CH_4^+$ and $^{13}CH_3D^+/^{12}CH_4^+$ are obtained. $^{13}CH_3D^+$ is measured at a count rate of
476 ~ 6,000 to 10,000 cps (depending upon sample size). Twenty blocks composed of twenty 30-s
477 integration cycles are used for these ratios. In the second setting, the magnet current is shifted to
478 place $^{12}CH_2D_2^+$ (mass = 18.04385 amu) in the axial collector. In addition, the continuously
479 variable collector slits are adjusted to bring the $^{12}CH_4^+$ beam into coincidence with the mass-17
480 and mass-18 beams (only the slit is migrated across the major beam, collectors remain in fixed
481 position). In this setting $^{12}CH_3D^+/^{12}CH_4^+$ and $^{12}CH_2D_2^+/^{12}CH_4^+$ are measured (Figure 5). Typical
482 count rates for measurements of $^{12}CH_2D_2^+$ are ~ 200 to 300 cps. Forty blocks of twenty 30-s
483 integrations are used for these ratios. A 25 ns dead-time correction, although unnecessary at the
484 count rates used, is applied to the electron multiplier. The sample and reference gas bellows are
485 adjusted to balance the ion current intensities between each measurement cycle, enabling long-
486 duration measurements.

487 Internal precision is consistent with counting statistics, yielding typical measurement
488 uncertainties of +/−0.15‰ and +/− 0.35‰ 1se for $\Delta^{13}CH_3D$ and $\Delta^{12}CH_2D_2$, respectively.
489 Measurement uncertainties for $\delta^{13}C$ (VPDB) and δD (VSMOW) are typically 0.003 and 0.02‰
490 1se, respectively. The accuracy of these methods has been assessed using inter-laboratory
491 comparisons and the mixing experiments shown in Figure 2 (Young et al. 2016). In addition to
492 these previous assessments, we report here measurements of gases equilibrated at known

493 temperatures in order to demonstrate further the accuracy of $\Delta^{13}CH_3D$ and $\Delta^{12}CH_2D_2$
494 measurements relative to theory (section 4.1). External 1σ precision for $\delta^{13}C$, δD, $\Delta^{13}CH_3D$, and
495 $\Delta^{12}CH_2D_2$ is approximately 0.1‰, 0.2‰, 0.2‰ and 0.6‰, respectively, based on replicate
496 samples.

497 **4. Laboratory Studies**

498 *4.1 Isotope exchange experiments – assessing accuracy*

499 The accuracy of our measurements was initially assessed through mixing experiments and inter-
500 laboratory comparisons (Young et al. 2016). Because there are at the time of this writing no
501 other data for CH_2D_2 at natural abundances, further assessment is justified. We addressed further
502 the accuracy in both $\Delta^{12}CH_2D_2$ and $\Delta^{13}CH_3D$ by analyzing products of the heating experiments in
503 which intra-species equilibration by isotope exchange is promoted by both temperature and the
504 presence of a platinum catalyst (Table 1). Our results are compared with theory (Equations 12
505 and 13). Figure 6 shows the results for $\Delta^{13}CH_3D$ vs. equilibration temperature. Methane
506 synthesis experiment products were included in the plot as well. The high-temperature catalyzed
507 silane reaction products (600^{o}C) and the platinum-catalyzed equilibration experiments are all
508 within analytical uncertainties of the theoretical relationship between $\Delta^{13}CH_3D$ and T; the
509 equilibration experiments match theory. The 90^{o}C Sabatier reaction product also matches the
510 theory curve although it could be argued that this datum should be excluded because the gas is
511 grossly out of equilibrium in $\Delta^{12}CH_2D_2$ (see below). Indeed the lower-temperature 70^{o}C reaction
512 product is far from expected equilibrium in $\Delta^{13}CH_3D$ as well as in $\Delta^{12}CH_2D_2$. Similarly,
513 measured $\Delta^{12}CH_2D_2$ values from the catalyzed exchange experiments and the 600^{o}C silane
514 reaction products agree with the theoretical relationship between $\Delta^{12}CH_2D_2$ and T (Figure 6).

515 *4.2 Abiotic synthesis experiments – the $^{12}CH_2D_2$ signature of abiotic methane synthesis*

Results of the Sabatier reaction experiments and the $Si_5C_{12}H_{36}$ decomposition experiments are shown in Figure 7 and listed in Table 1. While the experiments differ in detail, the overall pattern that emerges is one in which large deficits in $^{12}CH_2D_2$ relative to equilibrium and rather smaller deficits in $^{13}CH_3D$ relative to equilibrium typify abiotic methane formation in the laboratory. In fact, $\Delta^{13}CH_3D$ values are broadly consistent with the temperatures of formation although as a rule precise temperatures are not faithfully recorded at T < 600°C. The Sabatier reaction run at 90°C shows a deficit in $^{12}CH_2D_2$ but the $\Delta^{13}CH_3D$ value is consistent with the methane formation temperature within analytical uncertainties (Figure 6). However, at 70°C, the $\Delta^{13}CH_3D$ value is too low by about 1 ‰. At 300 to 400°C values for $\Delta^{12}CH_2D_2$ in the gases produced by silane decomposition are still low by many per mil compared with equilibrium and $\Delta^{13}CH_3D$ values are low by typically ~1 ‰ relative to equilibrium. Two silane decomposition experiments were conducted in the absence of a metal catalyst, and in both cases $\Delta^{13}CH_3D$ values are lower than with the catalyst at the same temperatures by ~ 1/2 ‰ (Table 1). In section 4.4 we investigate the causes of this overall pattern of kinetic isotope effects.

4.3 Methanogens in the laboratory

Methane produced by axenic *M. barkeri* and *M. acetivorans* at 30°C by the reaction $4CH_3OH \rightarrow 3CH_4 + CO_2 + 2H_2O$, and *M. thermolithotrophicus* grown at 65°C by the reaction $HCO_3^- + 4H_2 + H^+ \rightarrow CH_4 + 3H_2O$ all show marked kinetic isotopologue effects. Relatives of these methanogens have been identified in the South African mines of this study. In each of the three experiments deficits in $^{12}CH_2D_2$ comparable in magntiude to those produced in the abiotic experiments are observed (Figure 8). At 30°C, the kinetically-controlled deficits in $^{13}CH_3D$ of up to 10‰ are more extreme than those observed in the abiotic experiments. Negative $\Delta^{12}CH_2D_2$ values are evidently characteristic of microbial methane produced in the laboratory under favorable conditions for methanogen growth.

Previous work on $\Delta^{13}CH_3D$ values in microbially-produced methane has identified instances of equilibrium or near-equilibrium $\Delta^{13}CH_3D$ values as well as instances of kinetic control like that shown in the cultures presented here (Stolper et al. 2015; Wang et al. 2015). Our results show that kinetic depletions in $^{13}CH_3D$ are accompanied by even larger deficits in $^{12}CH_2D_2$ relative to equilibrium.

4.4 Kinetic signatures of CH_4 formation – the role of quantum tunneling

In order to gain some understanding of the kinetic effects associated with abiotic methane production, a reaction network representing the formation of methane on metal surfaces was constructed (Figure 9). We used the reaction scheme for FTT synthesis on a cobalt (Co) catalyst suggested by Qi et al. (2014). While we use CO as the source of carbon because the elementary steps in this reaction are well studied, methanation of CO_2 can occur by conversion first to CO with the subsequent steps being the same as those for direct methanation of CO (Wang et al. 2011). The kinetic model presented here is therefore relevant to methane production from CO_2 as well. We added isotope exchange between methane molecules on the surface, desorption and adsorption of CH_4 gas, and attack of CH_4 by OH to the elementary steps leading to methane formation. The set of reactions can be represented by these basic reactions and their isotopically-substituted equivalents:

$$
\begin{aligned}
&CO_g \rightarrow CO^* \\
&H_{2\,g} \rightarrow 2H^* \\
&CO^* + H^* \rightarrow HCO^* \\
&HCO^* + H^* \rightarrow HCOH^* \\
&HCOH^* \rightarrow CH^* + OH^* \\
&CH^* + H^* \rightarrow CH_2{}^* \\
&CH_2{}^* + H^* \rightarrow CH_3{}^* \\
&CH_3{}^* + H^* \rightarrow CH_4{}^* \\
&OH^* + H^* \rightarrow H_2O_g \\
&CH_4{}^* + OH^* \rightarrow H_2O^* + CH_3{}^* \\
&CH_4{}^* \rightleftarrows CH_4{}^* \\
&CH_4{}^* \rightarrow CH_{4g} \\
&CH_{4g} \rightarrow CH_4{}^*
\end{aligned}
\tag{16}
$$

where a superscript * signifies a surface-adsorbed species and a subscript g refers to a gas species. With all isotopologues and isotopomers the model consists of 124 species and 796 reactions. The rate constants for the reactions are of the form

$$k_f = Q_{\mathrm{Tun}} \frac{k_b T}{h} \frac{q^+}{\prod_r q_r} \left(\frac{-Ea}{k_b T} \right) \tag{17}$$

where k_b is the Boltzmann constant, h is the Planck constant, E_a is the activation energy, q_r are the partition functions for reactant species r, $q^{\mp}$ is the partition function for the transition state, and Q_{Tun} is a correction for quantum tunneling. The 124 ordinary differential equations comprising the model were solved numerically using the Lawrence Livermore ordinary differential equation solver (DLSODE). Activation energies for the methane formation reactions were taken from Qi et al. (2014). Values for E_a for the reaction CH_4 + OH were taken from Haghnegahdar (2015).

Pre-exponential terms in Equation (17) are dominated by the translational partition functions. We therefore used the 2D or 3D translational partition functions

570 $$\frac{q}{l^D} = \left(\frac{2\pi k_b T}{h^2} \right)^{D/2} \quad (18)$$

571 as appropriate to estimate the pre-exponential terms for Equation (17) (Baetzold and Somorjai
572 1976) where D is 2 for surface species and 3 for species in the gas phase and *l* is the length
573 dimension. In the absence of detailed information about all of the transition states involved in the
574 reaction network, we used the sum of the masses of the reactants as an estimate for the transition
575 states, a method known to give reasonable values. For example, using this scheme the H/D
576 kinetic isotope effect (KIE) obtained in our code for the reactions $HCO^* + H^* \rightarrow HCOH^*$ and
577 $HCO^* + D^* \rightarrow HCOD^*$ is 1.98 while the value given by Qi et al. is 1.93. Similarly, for the
578 reactions $HCOH^* \rightarrow CH^* + OH^*$ and $HDOD^* \rightarrow CD^* + OD^*$ our calculated KIE is 1.02 while
579 that from Qi et al. is 1.004. Overall we estimate an accuracy in KIE values relative to the fiducial
580 density functional theory calculations of ~ 2 to 5%. We note that variations in activation energies
581 for the surface catalyzed steps in our reaction network exhibit greater ranges in the literature than
582 our estimate in accuracy uncertainty.

583 In the absence of more detailed information, rate constants for isotope exchange between
584 methane molecules on the metal surface are taken to be 10^{12} s^{-1}. The rate constant for desorption
585 of methane is set at 10^2 s^{-1} and we did not include an isotope effect from desorption. Re-
586 adsorption was excluded from the results presented here. The exact values for these constants do
587 not affect the initial rate-limited isotope effects but they instead control the rate at which the
588 methane gas progresses from kinetic to equilibrium states of isotopic bond ordering. The values
589 used in our calculations give rates of equilibration consistent with our laboratory results.

590 We found that the kinetic model as described above when Q_{Tun} is unity cannot explain our
591 experimental data for methane formation. In particular, the calculated kinetically-controlled
592 values for $\Delta^{13}CH_3D$ are more negative, or less positive, than our experiments and the calculated
593 kinetic values for $\Delta^{12}CH_2D_2$ are considerably (by an order of magnitude at low temperatures) less

negative than in our experiments (Figure 7). The failure of the classical model to explain the large deficits in $^{12}CH_2D_2$ is a general result that arises because classical kinetics do not depart profoundly from the rule of the geometric mean (Bigeleisen 1955). The latter is a rough approximation in which fractionation factors for multiply-substituted species are similar to products of fractionation factors for the corresponding singly-substituted species with the remainder being thermodynamic effects. For example, where the $^{13}CH_3D/^{12}CH_4$ kinetic fractionation factor is of order 0.999 (−1‰), one expects that the $^{12}CH_2D_2/^{12}CH_4$ fractionation effect should be roughly 0.999^2 (−2‰), and so forth (where we assume the D/H fractionation dominates over the $^{13}C/^{12}C$ fractionation). Inspection of the classical kinetic effects (open stars in Figure 7) shows this to be approximately the case in our kinetic model. For this reason the magnitude of the classical CH_2D_2 kinetic fractionation is constrained to be on the order of a few per mil where the $^{13}CH_3D$ effect is also on the order of several per mil. This is not what we observe.

However, the de Broglie wavelength of hydrogen atoms at relevant temperatures is on the order of 1×10^{-10} meters and the typical quantum tunneling length scale for reactions involving the C-H bond is ~ 0.4×10^{-10} meters (Krishtalik 2000). Tunneling should therefore be an important process affecting rate constants for the reactions involving insertion of a hydrogen or a deuterium atom. In order to add this tunneling correction we used the prescription for Q_{Tun} after Bell (1959):

$$Q_{\mathrm{Tun}} = \frac{\alpha\ \exp(\alpha-\beta)}{(\alpha-\beta)} - \frac{\beta}{\alpha-\beta} \tag{19}$$

where

$$\alpha = \frac{E_a}{k_b T} \tag{20}$$

and

$$\beta = \frac{2a\pi^2(2mE_a)^{1/2}}{h}. \quad (21)$$

In equation (21) a is the tunneling length scale (tunneling distance = $2a$, Figure 10) and m is the mass of the tunneling particle. Equation (19) is valid when the energy of the particle is well below the top of the energy barrier and where departures from classical behavior are relatively large (when $\alpha > \beta$) (Bell 1980). In the present calculations $\alpha >> \beta$.

The experimental data for methane formation by the metal-catalyzed Sabatier reaction and by silane decomposition are explained within reasonable experimental and computational uncertainties by incorporating the tunneling correction in Equation (19) into the H and D additions in the reaction network. This fit is obtained by using $a_H = 0.3\times10^{-10}$ for H and $a_D/a_H = 1.005$. A longer tunneling length scale for D rather than H is expected (Limbach et al. 2006). Figure 10 shows the relationships between the length scale for tunneling and activation energy in the context of a Marcus-theory representation of the reactions of interest. We note that the state of the hydrogen and deuterium atoms is not known *a priori* so the values for a_D and a_H, while accounting for the relative probabilities of tunneling for these species, may not be strictly accurate representations of the physical tunneling distances. Nonetheless, we can evaluate the plausibility of these values. For example, if we approximate the energy barrier in Figure 10 as a parabola with the expression $(E_a - E) = f(\xi - \xi^*)^2$ where ξ is the reaction coordinate and ξ^* is the position of the barrier center, we arrive at $a = \xi - \xi^* = \sqrt{E_a / f}$ where $E = 0$ to show that $a_D/a_H = 1.005 = \sqrt{E_a(D)/E_a(H)}$. The differences in activation energies represented by a_D/a_H can be assessed by rewriting this relationship as $(a_D/a_H)^2 = (E_a + \sqrt{m_H/m_D}\Delta E)/(E_a + \Delta E)$ where we use the square root of the inverse of the atomic masses for H and D to relate their respective energy offsets (e.g., due to zero-point energies) from a fixed activation energy barrier maximum (E_a, Figure 10). With a typical activation energy in our reaction network of $\sim5\times10^{-20}$ J (30 kJ/mol) for H or D addition and $a_D/a_H = 1.005$ we obtain $\Delta E = 0.033E_a = 1.65\times10^{-21}$ J. This energy

641 corresponds to a vibrational frequency of 5 $\times 10^{-12}$ s^{-1} (170 cm^{-1}), a value that agrees with other
642 estimates for adsorbed hydrogen to within a factor of 2 or 3 (Yu et al. 2009). The constants used
643 in the tunneling correction appear reasonable.

644 The kinetic model, inclusive of tunneling, produces methane with $\delta^{13}C$ values of between
645 −41‰ and −42‰ relative to the carbon substrate. The product methane δD values are −795‰
646 and −640‰ at 30 and 300°C, respectively, relative to the reactant hydrogen. Values for δD
647 without tunneling are closer to ~ −550‰. Clearly, to reproduce the δD values of natural samples,
648 another step involving D/H isotope exchange between methane and other sources of hydrogen
649 would have to occur. Inter-species isotope exchange before and after desorption from the metal
650 catalyst is not included in the model at present. This exchange could explain why the depletion in
651 $^{12}CH_2D_2$ observed in natural samples (~ −10‰, see below) is not as extreme as that seen in the
652 laboratory (< ~ −50‰).

653 With the tunneling correction the large $^{12}CH_2D_2$ depletions relative to stochastic in the
654 experiments are explained, as are the comparatively minor departures of $^{13}CH_3D$ from
655 equilibrium, and the overall temperature dependence in both (Figure 7). It appears, therefore, that
656 quantum tunneling by hydrogen is a signature of abiotic methane production. We note that in the
657 case of the silane decomposition reactions, the tunnel effect would be manifest in the final step
658 where hydrogen is added to the methyl radical. The scatter in the silane decomposition data in
659 Figure 7 is an indication that more detailed work will be required in the future to understand the
660 influences of temperature, catalysis, and other factors on the kinetics of this process.

661 The cause of the large kinetic isotopic effects in methane gas produced by methanogens
662 under the conditions that obtained in our laboratory cultures may also involve quantum tunneling
663 of hydrogen (Klinman 2003). If so, it may be possible for methanogens to produce methane with
664 $\Delta^{12}CH_2D_2$ signatures resembling those of abiotic gas. An important distinction between the
665 kinetic effects exhibited by CH_4 produced in our axenic laboratory cultures and CH_4 produced by

abiotic reactions is that the former displays more negative $\Delta^{13}CH_3D$ values for a given $\Delta^{12}CH_2D_2$ value (compare Figures 7 and 8). This feature of methanogenesis may indicate that tunneling is less important relative to classical kinetic effects during microbial methane production.

Alternatively, the low $\Delta^{12}CH_2D_2$ values produced by microbial methanogenesis in the laboratory could be expressions of "combinatorial" effects (Yeung 2016). This purely statistical effect with an apparent biasing against D-D pairings arises when the four indistinguishable hydrogen atoms comprising the product methane molecule are derived from two or more distinct isotopic reservoirs or assembled with different D/H fractionation factors, both being more likely for enzymatic processes. The magnitude of the effect scales roughly quadratically with the sizes of the disparities in isotopic ratios of the reservoirs or fractionation factors. For example, if one of the four hydrogen positions was derived from a reservoir with a D/H twice that of the others, the result would be a $\Delta^{12}CH_2D_2$ value of −40 ‰ (Röckmann et al. 2016), comparable to the values observed in the culture experiments (Figure 8). In the case of unequal fractionation factors, if the D/H fractionation factors for four hydrogen addition steps producing CH_4 were 1.00, 1.00, 0.50 and 0.50, then the predicted $\Delta^{12}CH_2D_2$ value is −37‰, also similar to the most negative values in Figure 8. The effect on $\Delta^{13}CH_3D$ would only be 0.01‰. In general, the combinatorial effect should minimally influence $\Delta^{13}CH_3D$ values (Yeung 2016), suggesting that these statistical effects should work against correlations between $\Delta^{12}CH_2D_2$ and $\Delta^{13}CH_3D$. The apparent correlation between $\Delta^{12}CH_2D_2$ and $\Delta^{13}CH_3D$ defined by the culture data suggest that classical kinetic effects, in addition to tunneling and/or purely statistical effects, may be playing an important role in the microbial CH_4 isotopologue signatures shown in Figure 8.

The combinatorial effects are general and could in principle apply to abiotic as well as enzymatic formation pathways. However, the differences in fractionation factors or differences in D/H of isotopic reservoirs necessary to explain the observed negative $\Delta^{12}CH_2D_2$ values are on

690 the order of a factor of 2. These seem to be too extreme for abiotic pathways for methane
691 formation.

692 **5. Applications to Natural Samples**

693 Results for all natural samples reported here are listed in Table 1. Typical methane
694 concentrations for the gas samples can be found in the references sited in section 3.1. The bulk
695 isotopic compositions of the various samples are shown in Figure 11 together with approximate
696 boundaries for microbial, thermogenic, abiotic gas seeps, and abiotic methane discharging from
697 ground water. The gases span typical global ranges in both $\delta^{13}C$ (VPDB) and δD (VSMOW)
698 (Etiope et al. 2011; Etiope and Sherwood Lollar 2013). Generally speaking, the isotopic
699 compositions of the gases comport with their nominal provenance assignments. These same
700 gases in $\Delta^{12}CH_2D_2$ vs. $\Delta^{13}CH_3D$ space (Figure 12) can be broadly categorized into three groups:
701 1) those samples exhibiting isotopic bond ordering equilibrium, 2) those with clear negative
702 digressions from bond-order equilibrium, and 3) those with clear positive excursions from
703 equilibrium.

704 *5.1 Natural samples exhibiting equilibrium – thermometry applications*

705 A useful aspect of employing two multiply-substitued isotopologues is that the condition of intra-
706 species equilibrium becomes immediately apparent; the temperatures derived from samples in
707 which both $\Delta^{12}CH_2D_2$ and $\Delta^{13}CH_3D$ are consistent with equilibrium are more robust. In cases of
708 intra-species equilibrium the need to verify the derived temperatures by comparisons with prior
709 expectations is obviated. This is important because in many cases prior expectations for
710 temperatures of formation are based on indirect evidence such as thermal models, assumptions of
711 inter-species or inter-phase isotopic exchange equilibrium, or geochemical estimates for maturity,
712 and these indicators do not always agree (see below).

713 *Chimaera*: Samples from Chimaera are within error (based on external reproducibility) of
714 equilibrium (Figure 12). The three measurements define a temperature based on $\Delta^{13}CH_3D$ of
715 128°C +11/-10 (1σ). The temperature obtained with the somewhat less precisely determined
716 average $\Delta^{12}CH_2D_2$ is 129°C +16/-14 (1σ). These temperatures are significantly greater than the
717 estimates obtained by assuming that CH_4 and H_2 gas are in hydrogen isotopic equilibrium. Using
718 the D/H exchange calibration of Bottinga (1969), the H_2 D/H values from Etiope et al. (2011),
719 and the CH_4 D/H values reported here, one obtains a temperature of 43°C (Table 1). While the
720 samples of H_2 and CH_4 used for the temperature calculation were not obtained at the same time, a
721 similar result was reported by Etiope et al. (2011). Because the combination of $\Delta^{12}CH_2D_2$ and
722 $\Delta^{13}CH_3D$ indicates intra-methane equilibrium, we interpret the discrepancy in intra-species vs.
723 inter-species temperatures to be the result of isotopic disequilibrium between CH_4 and H_2.
724 The isotopic compositions of coexisting C1-C5 alkanes, the presence of CO_2 gas and N_2 gas
725 derived from mature organic matter, the molecular C1-C5 Schulz-Flory distribution, and the
726 existence of mature potential source rocks have been used to suggest that a thermogenic
727 component exists in the Chimaera gas (Etiope et al. 2011), and it could be argued *a priori* that the
728 $\Delta^{12}CH_2D_2$ and $\Delta^{13}CH_3D$-derived temperatures are compromised by this mixing. We can test this
729 hypothesis with the resolved $\Delta^{12}CH_2D_2$ and $\Delta^{13}CH_3D$ measurements. For this purpose we first
730 assume "typical" δD and $\delta^{13}C$ values for the thermogenic and abiotic endmembers with formation
731 temperatures of ~160°C and ~35°C, respectively, represented by thin solid lines in Figures 13 and
732 14. If both gases are in bond-order equilibrium at the time of their formation (a disequilibrium
733 isotopic bond order case is also shown in Figure 14), the mixing curve is just slightly below the
734 equilibrium curve in $\Delta^{12}CH_2D_2$ vs. $\Delta^{13}CH_3D$ space (Figure 14); clear deviations from the
735 equilibrium curve due to mixing would not be expected in this case because the difference in δD
736 between the gases is not large enough (Figure 13). However, if the isotope bond ordering in the
737 Chimaera CH_4 were indeed due to mixing between a low-temperature abiotic component and a

738 thermogenic component, the gas would have to be dominantly thermogenic (>80%) based on the
739 high temperature recorded by the relative abundances of both mass-18 isotopologues (Figure 14).
740 This conclusion is not sensitive to the exact temperatures involved. As an illustration, we
741 consider several possible mixing scenarios in Figure 15. Three distinct mixing curves are shown
742 in Figure 15, each marked with white circles showing 10% increments of mixing. Matching the
743 measured Chimaera values by mixing of abiotic gas formed at 80°C with a higher-temperature
744 thermogenic component formed at ~180°C would still require that the thermogenic component
745 comprises 70 to 80% of the Chimaera gas (Figure 15). Previous work has suggested only 10 to
746 20% for the mixing ratio of the thermogenic component. Of course, mixing between gases formed
747 at similar temperatures (within 20 degrees of one another) and with relatively similar δD values
748 cannot be ruled out in any mixing ratio. Nonetheless, the temperature of the abiotic component is
749 constrained by the plausible amounts of thermogenic gas in the mixture. Mixing between a
750 120°C abiotic gas with a 180°C thermogenic gas would suggest that Chimaera CH_4 consists of at
751 least ~40% thermogenic gas (Figure 15). The mixing ratio of thermogenic gas required by the
752 data decreases as the inferred temperature of the abiotic component increases. In all cases where
753 the thermogenic methane is thought to be the subordinate component, as suggested by the bulk
754 isotope ratios of the Chimaera methane, the $\Delta^{12}CH_2D_2$ and $\Delta^{13}CH_3D$ data require that the abiotic
755 component formed or equilibrated at high temperatures of > ~ 120°C and ≤ 140°C (allowing for a
756 sizable but still subordinate thermogenic component for the lower limit and the uncertainty in the
757 calculated equilibrium temperature for the upper limit), or that the gas is in the main thermogenic.
758 Since the bulk isotope ratios of the Chimaera methane would be unusual for a thermogenic gas
759 (higher in $\delta^{13}C$ and δD), the $\Delta^{12}CH_2D_2$ and $\Delta^{13}CH_3D$ values are best interpreted as being
760 dominated by an abiotic gas component formed at 120°C to 140°C.

761 This temperature range from the $\Delta^{13}CH_3D$ and $\Delta^{12}CH_2D_2$ data is higher than estimates for
762 ambient temperatures at depth today. The modern geothermal gradient suggests that the current

maximum temperatures in the ophiolite nappe, where methane is thought to originate, is ~ 80°C (Etiope et al. 2011). Because the Chimaera sampling site is far removed from known hydrothermal systems in an area of comparatively low heat flow for the region (Ilkisik 1995; Aydin et al. 2005), intra-species temperatures of 120 to 140°C suggest CH_4 formed during a different era where temperatures were higher, perhaps resulting from the exothermic properties of the serpentinization itself (Schuiling 1964; Allen and Seyfried Jr. 2004) or during emplacement of the ophiolite near the high-temperature metamorphic sole (shear zone) (Etiope et al. 2016). The continuous exposure of the gas to ultramafic rock surfaces with their potentially catalytic properties may be one factor contributing to its eventual intra-species equilibration.

The conclusion from the Chimaera methane mass-18 isotopologue data is that the major component of the methane gas effusing at this site is abiotic and formed at about 120°C to 140°C. We also conclude from these data that CH_4-H_2 D/H thermometry yields spurious temperatures due to inter-species disequilibrium.

Marcellus and Utica shales: Methane gases from the Marcellus and Utica shales are also possessed of equilibrium distributions of the mass-18 isotopologues and therefore reliable temperatures of formation or equilibration are obtained (Figure 12). We calculate an equilibrium temperature of 145°C +6/–6 using the data in Table 1 (1 se for the single analysis and using the more precise $\Delta^{13}CH_3D$ value). Our result for the Marcellus gas agrees with the 147°C +25/–22 found by Wang et al. (2015) using $\Delta^{13}CH_3D$ alone as measured by tunable laser spectroscopy. Our temperature is considerably lower than the 179°C to 207°C found by Stolper et al. (Stolper et al. 2014) using unresolved $\Delta(^{13}CH_3D+^{12}CH_2D_2)$ and it is also lower than the thermal model for methane generation described by these authors (see above). Results reported here suggest that methane did not form, or last equilibrate, at peak burial temperatures if thermal models cited above are correct. We obtain a temperature of 155°C +10/–9 for the Utica Shale gas, suggesting a slightly higher temperature for the gas from this stratigraphically deeper reservoir (Figure 12).

In this instance the temperature of formation of the shale-derived methane, fortified by the fact that both mass-18 isotopologues are consistent with thermodynamic equilibrium, requires revision of the temperature of methane formation in the source rocks.

Birchtree Mine: The methane from the Birchtree Mine yields an equilibrium (i.e., concordant) temperature of 16^{o}C +6/–4 (Figure 12). This temperature is similar to the 20 to 23^{o}C water temperature in the mine. The bulk isotopic composition of this gas is consistent with microbial methanogenesis. The low temperature similar to the current water temperature is further indication that this gas is affected by extant biological processing in the environs of these waters at shallow depths. This conclusion is bolstered by the presence of active methanogens in the Thompson mine on the same property. The fact that CH_4 from the Birchtree mine is in intra-species isotopic bond order equilibrium, has bulk isotope ratios suggestive of a significant microbial component, and formed at temperatures consistent with the present-day water temperatures, all suggest that microbial processing in natural settings can lead to equilibrium isotopic bond ordering.

5.2 Natural samples exhibiting disequilibrium

The CH_4 samples described in this section exhibit different degrees of isotopic bond order disequilibrium. The gases with the greatest degrees of disequilibrium, including those sampled at Kidd Creek, Tau Tona, and Cabeco de Vide, have $\Delta^{12}CH_2D_2$ and $\Delta^{13}CH_3D$ characteristics resembling those of methane produced by abiotic synthesis in the laboratory (section 4.2). The Masimong and Beatrix samples have smaller but still substantial negative excursions in $\Delta^{12}CH_2D_2$ relative to equilibrium. The Beecher Island gas shows a small but important departure from equilibrium. Kloof and Acquasanta Terme samples display apparent excesses in $^{12}CH_2D_2$ rather than deficits that suggest a process of isotope fractionation or perhaps mixing. In all of these cases, temperatures of formation cannot be obtained quantitatively. However, comparisons with

812 our experimental data and consideration of the geological context for each sample lead to new
813 insights into the provenance of methane at each site.

814 *Beecher Island*: The Beecher Island gas field sample exhibits a small but resolvable
815 depletion in $^{12}CH_2D_2$ relative to equilibrium that signifies disequilibrium (Figure 12). This
816 depletion casts doubt on the veracity of temperatures derived from isotope clumping. The small
817 but resolvable disequilibrium is a valuable example of how a temperature deduced from $\Delta^{13}CH_3D$
818 alone, that otherwise appears perfectly reasonable, may in fact be spurious and therefore
819 misleading. The Beecher Island bulk δD and $\delta^{13}C$ values are well within the ranges expected for
820 a microbial gas but also overlap values for some thermogenic gases (Figure 11). However, at face
821 value the temperature from $\Delta^{13}CH_3D$ is 142°C +/-8 while the practical upper temperature limit for
822 microbial processing of methane is ~ 80°C (Valentine 2011), growth of methanogens in the
823 laboratory at higher temperatures of 122°C not withstanding (Takai et al. 2008). The $\Delta^{13}CH_3D$
824 temperature value is therefore clearly higher than expected for a "biogenic" (meaning microbial
825 in this context) gas, but this disagreement alone is not sufficient evidence to reject the clumping
826 temperature. Rather, the lack of mass-18 isotopologue equilibrium (i.e., concordant
827 temperatures) is evidence that the temperature obtained from clumped isotopes should be
828 considered unreliable, and that further study is required. For example, the face-value $\Delta^{13}CH_3D$
829 temperature of ~ 140°C could suggest that the Beecher Island gas is not "biogenic" (i.e.,
830 microbial) but rather thermogenic, and therefore similar to gases from deeper in the Niobrara
831 Formation. However, the presence of disequilibrium concentrations of the rare isotopologues cast
832 doubt on this conclusion. The ability to identify isotopologue disequilibrium even where the
833 temperature derived from $\Delta^{13}CH_3D$ alone is plausible is a considerable benefit afforded by these
834 data. Departures from equilibrium in both mass-18 methane isotopologues as a consequence of
835 microbial activity are consistent with our observations of methanogenesis in the laboratory

836 (Figure 8). Spuriously high $\Delta^{13}CH_3D$ temperatures due to isotopic bond order disequilibrium are
837 also consistent with previous reports (Wang et al. 2015) .

838 *Kidd Creek, Tau Tona, and Cabeço de Vide*: Dramatic departures from equilibrium are found
839 in methane effusing from relatively cool waters from the deep mines and from the Cabeço de
840 Vide spring. Three distinct localities, including Kidd Creek, Tau Tona, as well as Cabeço de
841 Vide, representing two distinct Precambrian shields and an unrelated ultramafic complex, all
842 exhibit large depletions in $\Delta^{12}CH_2D_2$ of up to ~ 25‰ relative to equilibrium (Figure 12). Two
843 additional Witwatersrand mine samples, from Masimong and Beatrix, also show substantial
844 negative excursions in $\Delta^{12}CH_2D_2$ relative to equilibrium (Figure 12). The bulk isotopic
845 compositions of these disequilibrium samples are all very different from one another (Figure 11).

846 The most extensively sampled of these is the Kidd Creek mine. Water temperatures in the
847 mine are ~ 20°C to 30°C, and the $\Delta^{13}CH_3D$ values for all of the Kidd Creek samples, from both
848 the 7850 and 9500 foot levels and collected over a period of 8 years, are broadly consistent with
849 this temperature, although with many measurements scattered to somewhat higher apparent
850 temperatures near 50°C. The $\Delta^{12}CH_2D_2$ is highly variable from −10 ‰ to near equilibrium (Figure
851 12). The most $^{12}CH_2D_2$ depleted samples come from the deeper 9500 foot level of the mine
852 (Table 1). However, because the samples represent a time interval of nearly 8 years, we are able
853 to identify a time-dependence to the $\Delta^{12}CH_2D_2$ values that suggests that the disparate $\Delta^{12}CH_2D_2$
854 values are not a function of level in the mine but rather depend on the time of exposure to the
855 outside world. Sherwood Lollar (2002) reported the presence of abiotic-dominated CH_4 from the
856 6800 foot level. The $\delta^{13}C$ CH_4 and C1/C2+ values for the 6800 samples overlap those of the
857 9500 foot level. Both sets of samples were collected within months of borehole completion. In
858 contrast, the samples from the 7850 boreholes were sampled 5 years after completion and exhibit
859 lower $\delta^{13}C$ values (Table 1) and higher C1/C2+. Indeed, all of the methane isotope ratios are

860 varying with time at Kidd Creek. For example, Figure 16 shows covariation of δD, $\delta^{13}C$, and
861 $\Delta^{12}CH_2D_2$ with days since the borehole was drilled.

862 The question arises as to the commonality between the deep mine methane and the methane
863 degassing from the spring at Cabeço de Vide that results in low $\Delta^{12}CH_2D_2$ values. It seems likely
864 that the link is surface catalysis followed by preservation by entrainment in water at relatively
865 low temperatures. Like the abiotic gases from the Precambrian shields, the Cabeço de Vide
866 methane is likely to have been produced by FTT reactions involving metals. And, like the deep
867 mine gases, this gas was entrained in cool water. In each of these settings, it is possible that the
868 signature low $\Delta^{12}CH_2D_2$ values are preserved by the relatively low temperatures at which the CH_4
869 gases reside. While the $\Delta^{13}CH_3D$ values of the Kidd Creek methane samples are crudely
870 consistent with the inferred low-temperatures of formation, we demonstrated with experiments
871 (section 4.2) that where $\Delta^{12}CH_2D_2$ is greatly depleted, $\Delta^{13}CH_3D$ can also be in part kinetically
872 controlled in general (e.g., the 70°C Sabatier reaction, Figure 7). Therefore, we do not think that
873 the apparent $\Delta^{13}CH_3D$ temperature of ~ 150°C for the Cabeço de Vide sample can be taken as
874 reliable evidence that the gas was formed at such high temperatures. Nonetheless, more work
875 should be undertaken at this site because the similarity between the equilibrium temperature
876 obtained from the Chimaera samples and the Cabeço de Vide sample is intriguing.

877 *Masimong and Beatrix*: The Masimong and Beatrix gases are believed to be largely
878 microbial in origin at present (section 3.1), and among the deep mine gases, they exhibit the
879 closest approaches to equilibrium (superseded only by the Birchtree sample that is entirely
880 equilibrated and also dominated by microbial methanogenesis). This observation, in combination
881 with the time variability towards equilibrium over several years documented at Kidd Creek,
882 suggests that in all of the deep mines, methane was produced abiotically with telltale low
883 $\Delta^{12}CH_2D_2$ values caused by tunneling that are progressively erased by the incursion of biological

884 activity that drives the isotopic bond ordering in methane towards equilibrium. The data imply
885 that the microbial communities influence methane isotopic values once the boreholes are drilled.
886 At Beatrix, Tau Tona and Masimong archaea are estimated to comprise ~1.5% (Simkus et al.
887 2016), ~ 4% (Simkus et al. 2016), and 11% (this study), respectively, of the sampled (planktonic)
888 microbial communities. These archaeal communities are dominated by methanogens within the
889 Methanobacteria, Methanomicrobia, and methanogen-containing Thermoplasmata classes.
890 Anaerobic methane oxidizers within the ANME-1, ANME-2 and ANME-3 clades are also present.
891 PLFA (Simkus et al. 2016), molecular (DNA, RNA, protein), and enrichment experiments
892 (Magnabosca et al. 2016) have provided further evidence for anaerobic methane oxidation in
893 these deep mine environs. Therefore, the deep mines likely exhibit active methane cycles in
894 which methanogens produce methane and the ANME groups destroy methane by anaerobic
895 methane oxidation.
896 *Thermometry pitfalls*: The broad agreement between $\Delta^{13}CH_3D$ values and host water
897 temperatures for the deep mine methane gases exhibiting pronounced D-D bond order
898 disequilibrium is at once a useful property and a seductive pitfall. This relationship might prove
899 useful as a general indicator of formation temperature but might also be mistakenly used to infer
900 that $\Delta^{13}CH_3D$ is always a robust temperature indicator regardless of evidence for disequilibrium.
901 The progression of CH_4 isotopologue ratios with time at Kidd Creek is essentially vertical in
902 $\Delta^{12}CH_2D_2$ vs. $\Delta^{13}CH_3D$ space and trends toward equilibrium temperatures of ~ 30 to 50°C, within
903 ≤ ~ 20 degrees of the present-day water temperatures of ~ 23°C to 33°C (Figure 12). The
904 $\Delta^{13}CH_3D$ data for the Massimong, Beatrix, and Tau Tona mines are also crudely consistent with
905 the water temperatures of ~ 30°C. This rough agreement between host water temperatures and
906 temperatures derived from ^{13}C-D isotope clumping despite clear evidence for D-D isotopic bond
907 order disequilibrium is similar to the pattern obtained in the Sabatier reactions in the laboratory:
908 differences in H and D tunneling impart larger kinetic effects for $^{12}CH_2D_2$ than for $^{13}CH_3D$. The

909 agreement between expected temperatures and $\Delta^{13}CH_3D$ temperatures in these instances is in part
910 fortuitous, however. Relatively larges variations in $\Delta^{13}CH_3D$ of nearly 1‰ correspond to shifts
911 of only ~ 20 degrees in the vicinity of 30°C (Figure 12). At these temperatures, relatively sizable
912 kinetic effects in $\Delta^{13}CH_3D$ values have muted impacts on calculated temperatures. For
913 comparison, consider that a kinetically-induced 1‰ spread in $\Delta^{13}CH_3D$ values at temperatures >
914 100°C corresponds to temperature differences of ≥ 100 degrees. Therefore, because of the low
915 temperatures involved, the $\Delta^{13}CH_3D$ values for these samples might be taken as supporting
916 evidence for low temperatures of formation in general as deduced by other means but should not
917 be used as quantitative thermometers.

918 For example, the assumption of liquid H_2O-H_2 D/H isotope exchange equilibrium yields
919 relatively low temperatures of 30 to 33°C for the 7850 Kidd Creek samples and 44 to 56°C for the
920 9500 Kidd Creek samples (Table 1). These compare reasonably well with the ~ 20°C and ~ 30°C
921 water temperatures at 7850 and 9500 foot levels in the mine, respectively, especially in view of
922 the > 20 degree scatter observed where this thermometer has been applied at other localities (e.g.,
923 Proskurowski et al. 2006). The origin of H_2 gas in these geological settings by water-rock
924 reactions or by radiolysis argues for an approach to isotopic equilibrium between water and H_2
925 gas. The hydrogen isotope data for waters and H_2 gases are generally consistent with D/H
926 equilibration. On the other hand, CH_4 and H_2 D/H partitioning does not agree with these other
927 two temperature indicators, yielding apparent temperatures of 84 to 172°C (Table 1).
928 Comparison of the $\Delta^{12}CH_2D_2$ vs. $\Delta^{13}CH_3D$ systematics of the abiotic methane production
929 experiments with the $\Delta^{12}CH_2D_2$ vs. $\Delta^{13}CH_3D$ data from the deep mines, together with the inter-
930 species thermometry results, suggests that the best interpretation is that methane gases from the
931 Canadian shield and Witwatersrand Basin deep mines formed at temperatures ≤ 50°C and that
932 these gases are not in D/H equilibrium with their host waters or with the coexisting H_2 gas.

933 Sherwood Lollar et al. (2008) arrived at similar conclusions based on the inter-species D/H
934 partitioning and the kinetics of inter-species D/H exchange.

935 Deuterium-hydrogen isotope exchange disequilibrium between CH_4 and H_2 like that proposed
936 for the deep mine gases was also proposed above for the Chimaera gases based on disagreement
937 between the concordant, equilibrium $\Delta^{12}CH_2D_2$ vs. $\Delta^{13}CH_3D$ temperatures and the CH_4-H_2
938 exchange equilibrium temperatures at that site (Table 1). The prevalence of inter-species
939 disequilibrium suggests that D/H exchange is not a reliable thermometer for CH_4 formation. We
940 note that the e-fold timescale for hydrogen isotope exchange equilibration between water and
941 methane is ~ 1 Myr at 200°C (Sessions et al. 2004), suggesting that at temperatures of < 100°C
942 equilibration timescales may be on the order of ~10 Myr. None of the samples for which we have
943 δD values for both H_2O and coexisting CH_4 are in hydrogen isotopic equilibrium at the measured
944 water temperatures (Table 1). The inter-phase isotopic disequilibrium suggests that the CH_4 gas
945 has been in persistent contact with its host water for timescales of less than tens of millions of
946 years. Sequestration in relatively cool waters for timescales of less than 10^7 years explains the
947 preservation of disequilibrium isotopic bond ordering in all but one of the aqueous CH_4 samples
948 (the exception being the Birchtree gas that is evidently largely if not entirely microbial in origin).

949 *Abiotic – biotic gas mixing*: In earlier studies (Sherwood Lollar et al. 2007) it was proposed
950 that a trend in δD vs $\delta^{13}C$ space between nominally abiotic methane gas resembling Kidd Creek
951 and microbial gas resembling methane sampled at Masimong and Beatrix represents mixing
952 between typical microbial ("M") and abiotic ("A") gases. We can use $\Delta^{13}CH_3D$ and $\Delta^{12}CH_2D_2$ to
953 test this mixing scenario. The microbial-abiotic mixing proposed previously is shown in Figure
954 13 with the dash-dot-dash line. This mixing is shown in mass-18 isotopologue space in Figure 14
955 with the same line symbol. In this case we use the maximum deficit in $\Delta^{12}CH_2D_2$ exhibited by the
956 samples from Kidd Creek for the abiotic endmember and a microbial endmember that is assumed
957 to be equilibrated at 30°C (representing gas equilibrated at present-day water temperatures). The

point at which the mixing curve crosses the equilibrium curve in Figure 14 corresponds to a mixing ratio for the microbial component of 14%. For larger proportions of microbial gas, the large differences in δD between Kidd-Creek-like abiotic gas and microbial gas would result in large positive $\Delta^{12}CH_2D_2$ excursions from the equilibrium curve upon mixing. Since the gases from Masimong and Beatrix mines lie below the equilibrium curve, rather than above it, and yet exhibit bulk isotopic ratios suggesting large microbial components, we find that the mass-18 isotopologue data are not consistent with this mixing scenario. Mixing between this same microbial endmember used above and an abiotic component similar to the Chimaera gas in δD and $\delta^{13}C$ is also shown in Figures 13 and 14 with dotted lines. In this case the differences in δD are smaller, and so the mixing curve never crosses the equilibrium curve in Figrue 14. Although the dotted curve in Figure 14 more closely resembles the deep mine gases in $\Delta^{13}CH_3D$ and $\Delta^{12}CH_2D_2$, there is no evidence for a methane component resembling the Chimaera gas in the deep mine systems (Figure 13).

The failure of the "M" – "A" mixing model does not mean that the Kidd Creek gases with intermediate $\Delta^{12}CH_2D_2$ values are not the result of mixing between the gases with the lowest $\Delta^{12}CH_2D_2$ values and those with the highest, near-equilibrium values. All of the methane isotope data at Kidd Creek can be explained reasonably well by mixing between the two most extreme samples. The right-hand panel of Figure 16 shows a mixing curve through the data illustrating this point (this same curve is essentially vertical through the data in Figure 14). By extension, we suggest that the gases from Tau Tona may also be mixtures between abiotic gas with very low $\Delta^{12}CH_2D_2$ values and gases driven closer to equilibrium by microbial activity. Likewise, the low $\Delta^{12}CH_2D_2$ values of the Beatrix and Masimong gases may also be vestiges of the abiotic component, although disequilibrium resulting from microbial processing cannot be ruled out.

Kloof and Acquasanta Terme apparent excesses in $^{12}CH_2D_2$: Two methane samples lie above the equilibrium curve in Figure 12 rather than below it. These are the Witwatersrand Kloof Mine

sample and the sample from the Acquasanta Terme hyperalkaline spring. In both cases it is clear that a temperature obtained from $\Delta^{13}CH_3D$ would be incorrect. In general, positive $\Delta^{12}CH_2D_2$ displacements from the equilibrium curve can be attributable to either mixing of gases with disparate δD values or fractionation of the bulk isotopic composition of the gas without bond re-ordering (i.e., without bond rupture and reformation), as described above (Figure 3). We show in Figures 13 and 14 a mixing scenario that attempts to explain the isotopic composition of the Kloof mine methane, for example. In this model equilibrated thermogenic gas, seemingly required by the relatively low $\Delta^{13}CH_3D$ values for the Kloof gas, is mixed with an abiotic component to explain the relatively low δD values (Figure 13). Two different abiotic methane components are considered, one with very low $\Delta^{12}CH_2D_2$ values resembling the more primitive Kidd Creek gases, and the other equilibrated at 30°C, resembling the Kidd Creek gases driven towards isotope bond ordering equilibrium by microbial processing (Figure 14). The results are shown as dashed lines in both Figures 13 and 14. While not meant to be a quantitative fit to the data, one can see that positive excurisons in $\Delta^{12}CH_2D_2$ relative to equilibrium can be produced by such a scenario. A thermogenic component derived from breakdown of organics in the Witwatersrand Supergroup has been proposed in the past, but there is nothing in the geological setting of the Kloof Mine that constitutes compelling evidence for a thermogenic source. Similar circumstances obtain for the Acquasanta gas; there is no compelling evidence for a thermogenic component but one cannot be ruled out either.

An alternative explanation for the disequilibrium $\Delta^{12}CH_2D_2$ and $\Delta^{13}CH_3D$ values for these gases is that they were affected by a kinetic process that raised their bulk δD and $\delta^{13}C$ values, thus altering the stochastic reference frame for calculating the $\Delta^{12}CH_2D_2$ and $\Delta^{13}CH_3D$ values. In this case the distribution of rare isotopologues is no longer consistent with the bulk isotopic composition, resulting in spuriously high $\Delta^{12}CH_2D_2$ values relative to $\Delta^{13}CH_3D$ values. A simple but unlikely candidate is molecular diffusion (e.g., Figure 3). The latter is simple to model and

1008 serves as an illustration of the effect. We show such a model in Figure 17. In this case the initial
1009 gas is chosen to be equilibrated at 30°C and to have a bulk isotopic composition resembling the
1010 Birchtree gas. The model curves in Figure 17 show the evolution of the residual gas following
1011 Rayleigh distillation by molecular diffusion. While the calculation could explain both the Kloof
1012 and the Acquasanta gases in clumping space, the trend in bulk isotope ratio space is shallower
1013 than the trend defined by these data taken together. However, there is no reason to assume that
1014 the starting compositions for the two methane sites were the same. Therefore, it remains true that
1015 a process that fractionates the methane according to molecular weight could explain the positive
1016 $\Delta^{12}CH_2D_2$ deviations from the equilibrium curve as well as apparent increases in $\delta^{13}C$ with only
1017 modest increases in δD relative to other deep mine gases. A search for candidate processes
1018 would seem warranted. In all cases, the essential point is that clumped isotopes of these gases do
1019 not yield temperatures.

1020 **6. Discussion**

1021 The telltale signatures of catalyzed abiotic methane formation caused by the different tunneling
1022 behaviors of protium and deuterium is evidently preserved where methane is sequestered in
1023 ground waters (e.g., the deep mine gases and the Cabeco de Vide spring). This abiotic signature
1024 may never form at higher temperatures in some natural settings or may be erased with prolonged
1025 and direct exposure of CH_4 gas to rock surfaces (e.g., Chimaera). This relatively simple picture
1026 is modified substantially by microbial production and/or cycling of methane gas. The
1027 consequences of spatially-overlapping abiotic methane migration and microbial methane
1028 production and cycling is discussed below.

1029 *6.1 Biological processing of CH_4*

1030 Results of several studies of clumped isotopes in methane show that equilibrium in $\Delta^{13}CH_3D$ can
1031 occur with biological production of methane gas (Stolper et al. 2015; Wang et al. 2015). The

1032 factors governing the degree of isotope bond order equilibrium or disequilibrium in microbial
1033 CH_4 production are at present unclear, in part because the kinetic pathways are still matters of
1034 active investigation (Wongnate et al. 2016). Wang et al. (2015) used a Michaelis-Menton
1035 formulation for the kinetics of microbial methane production that highlights the potential
1036 reversibility of the enzymatic process. They linked the degree of reversibility to the availability of
1037 H_2. The concept of reversibility is consistent with the reversibility of archaeal methanogensis and
1038 anaerobic oxidation of methane (AOM) afforded by the methyl-coenzyme M reductase (MCR)
1039 common to organisms responsible for these two processes (Scheller et al. 2010), and
1040 enzymatially-driven $^{13}C/^{12}C$ equilibration in CH_4 by AOM has been reported previously
1041 (Ysohinaga et al. 2014). An open question is whether isotopic bond order equilibration can occur
1042 with only minor effects on bulk δD and $\delta^{13}C$ values by microbial processing of a reservoir of CH_4.
1043 Continuous production (methanogenesis) simultaneous with destruction (e.g., AOM) of CH_4 by
1044 the opposing effects of similar enzymatic activities operating in reverse directions (i.e.,
1045 production of CH_4 favoring light isotopes in concert with binding and destruction of CH_4 that also
1046 favors the lighter isotopes) may result in a near steady state in terms of bulk isotopic composition
1047 that resembles the original source of methane. Methane bonds would be remade by the
1048 methanogens in this environment and so could be driven to isotopic bond order equilibrium under
1049 the right conditions. The effect of microbial communities on methane isotope clumping is fertile
1050 ground for future research. For now, based on the CH_4 isotope data collected from the various
1051 sampling sites presented here, and the presence of both methanogens and methanotrophic archaea
1052 (ANME) in the systems approaching equilibrium, we conclude that microbial communities can
1053 process methane to produce equilibrium or near equilibrium isotopic bond ordering.

1054 *6.2 Competition between abiotic and biotic methane production*

1055 The picture that emerges from these studies is one in which abiotic methane can be reprocessed
1056 by microbial activity in some settings. Abiotic methane production results in significant

depletions in $^{12}CH_2D_2$ with more modest or even negligible depletions in $^{13}CH_3D$ relative to equilibrium both in the laboratory and in natural settings. The isotopologue signatures of catalyzed abiotic methane formation are evidently preserved where the gas is entrained in cool waters (e.g., Precambrian shield mine gases).

Microbial activity can produce large depletions in both $^{12}CH_2D_2$ and $^{13}CH_3D$ but can also lead to equilibrium $\Delta^{12}CH_2D_2$ and $\Delta^{13}CH_3D$ values. Methane gases effusing from fracture waters in the deep mines of the Precambrian shields have the significant deficits in $^{12}CH_2D_2$ and more modest depletions in $^{13}CH_3D$ that we attribute to abiotic methane formation. These pristine gases are subsequently prone to recycling and isotopic bond re-ordering as microbial communities colonize the fractures from which the gases are issuing over time. The equilibrium clumping signature at host water temperatures in the Birchtree mine sample may be an example of this process going to completion. A schematic representing this scenario to explain the deep mine gases is shown in Figure 18. The figure illustrates the spatial and temporal evolution of the microbial component to the methane gas budget in the rock fracture system as a consequence of opening a new drill hole.

7. Conclusions

The use of two mass-18 rare isotopologues of methane affords insights into the provenance of methane gases from a variety of natural settings. Where $\Delta^{12}CH_2D_2$ and $\Delta^{13}CH_3D$ values are inconsistent with thermodynamic equilibrium, temperatures of formation based on one or the other of these species must be considered with suspicion. However, the details of the disequilibrium isotopologue ratios provide important information about the history and even the formation mechanism of the gas. Without measurements of $\Delta^{12}CH_2D_2$ to go along with $\Delta^{13}CH_3D$ values, otherwise seemingly plausible temperatures obtained with $\Delta^{13}CH_3D$ values alone could easily be mistaken for true temperatures of formation. Several examples of this potential pitfall are described in this study.

Where $\Delta^{12}CH_2D_2$ and $\Delta^{13}CH_3D$ do yield concordant temperatures, representing isotopic bond order equilibrium, we find that these temperatures are sometimes at odds with temperatures inferred by indirect means. Equilibrium $\Delta^{12}CH_2D_2$ and $\Delta^{13}CH_3D$ temperatures that do not match those obtained by D/H exchange thermometry between CH_4 and H_2 and between CH_4 and H_2O suggest that CH_4 is not in D/H exchange equilibrium with either species in the samples studied here, calling into question the general use of inter-species D/H exchange as a reliable thermometer for methane formation except perhaps at higher temperatures than those encountered in this study.

The deficits in $^{12}CH_2D_2$ compared with equilibrium values in CH_4 gas made by abiotic reactions are sufficiently large as to point towards a quantum tunneling origin. Tunneling also accounts for the more moderate depletions in $^{13}CH_3D$ relative to equilibrium that accompany the low $^{12}CH_2D_2$ abundances. This tunneling signature of abiotic methane formation may prove to be an important tracer of abiotic methane formation, especially where it is likely to be preserved by dissolution of gas in cool hydrothermal systems. Eventual applications to methane on Mars are obvious. Mechanisms for erasing the kinetic signature of abiotic methane formation include recycling by biological activity and perhaps prolonged exposure of the gas phase to rock surfaces at temperatures of ~ 150^{o}C or greater.

The scenario of biological recycling of abiotic methane is a cautionary tale for assigning provenance to CH_4 in general. In the laboratory, methanogenesis produces disequilibrium isotopic bond order effects rivaling those produced by abiotic CH_4 production, although the effects for $^{13}CH_3D$ are larger and the effects for $^{12}CH_2D_2$ are smaller than in the abiotic gases. In natural settings, however, there is evidence for microbial cycling leading to equilibrium isotopic bond ordering. The conditions leading to isotopic bond order equilibrium in methane produced by, or acted upon by microbial communities requires further study.

Acknowledgements

This research has been supported by the Deep Carbon Observatory (Sloan Foundation), the National Science Foundation's EAR program (0948938 to EDY and DR and 1539023 to EDY), the Department of Energy (DE-SC0006623 to DR and EDY), Shell Projects and Technologies Inc. - Emerging Technologies Group, the ACS Petroleum Research Fund (54848-ND2 to EDY), the Carnegie Institution of Washington (DR), the Natural Sciences and Engineering Research Council of Canada (BSL, CS, OW), the Center for Dark Energy Biosphere Investigations, C-DEBI (IPR, DEL), and the NASA Astrobiology Institute (ARR, DEL). We thank Alvin Ly (UCLA) and Nate Monson (UCLA) for help in the laboratory. We benefited greatly from discussions early on in this project with Weifu Guo (Woods Hole Oceanographic Institution).

References Cited

Allen D. E. and Seyfried Jr. W. E. (2004) Serpentinization and heat generation: constraints from Lost City and Rainbow hydrothermal systems. *Geochemica et Cosmochimica Acta* **68**(6): 1347-1354.

Aydin I., Karat H. I. and Kocak A. (2005) Curie-point depth map of Turkey. *Geophysical Journal International* **162**: 633-640.

Baetzold R. C. and Somorjai G. A. (1976) Preexponential factors in surface reactions. *Journal of Catalysis* **45**: 94-105.

Bell R. P. (1959) The tunnel effect correction for parabolic potential barriers. *Transactions of the Faraday Society* **55**: 1-4.

Bell R. P. (1980). The Tunnel Effect in Chemistry. London, Chapman and Hall.

Bigeleisen J. (1955) Statistical mechanics of isotopic systems with small quantum corrections. I. General considerations and the rule of the geometric mean. *The Journal of Chemical Physics* **23**(12): 2264-2267.

Blamey N. J. F., Parnell J., McMahon S., Mark D. F., Tomkinson T., Lee M., Shivak J., Izawa M. R. M., Banerjee N. R. and Flemming R. L. (2015) Evidence for methane in Martian meteorites. *Nature Communications* **6:7399**.

Borgonie G., Linage-Alvarez B., Ojo A. O., Mundle S. O. C., Freese L. B., Rooyen C. V., Kuloyo O., Albertyn J., Pohl E., Cason E. D., Vermeulen J., Pienaar C., Litthauer D., Van Niekerk H., Van Eeden J., Sherwood Lollar B., Onstott T. C. and Van Heerden A. (2015) Eukaryotic opportunists dominate the deep-subsurface biosphere in South Africa. *Nature Communications* **6**: 8952.

Boschetti T., Etiope G. and Toscani L. (2013) Abiotic methane in the hyperalkaline springs of Genova, Italy. *Procedia Earth and Planetary Science* **7**: 248-251.

Bottinga Y. (1969) Calculated fractionation factors for carbon and hydrogen isotope exchange in the system calcite-carbon dioxide-graphite-methane-hydrogen-water vapor. *Geochemica et Cosmochimica Acta* **33**: 49-64.

Brown R. H., Soderblom L. A., Clark R. N., Jaumann R., Barnes J. W., Sotin C., Buratti B., Baines K. H. and Nicholson P. D. (2008) The identification of liquid ethane in Titan's Ontario Lacus. *Nature* **454**: 607-610.

Burruss R. C. and Laughrey C. D. (2010) Carbon and hydrogen isotopic reversals in deep basin gas: evidence for limits to the stability of hydrocarbons. *Organic Geochemistry* **41**(12): 1285-1296.

Cluff M. A., Hartstock A., MacRae J. D., Carter K. and Mouser P. J. (2014) Temporal changes in microbial ecology and geochemistry in producer water from hydralulically fractured marcellus shale gas wells. *Environmental Science & Technology* **48**: 6508-6517.

Cramer B. (2004) Methane generation from coal during open system pyrolysis investigated by isotope specific, Gaussian distributed reaction kinetics. *Organic Geochemistry* **35**: 379-392.

Cramer B., Krooss B. M. and Littke R. (1998) Modelling isotope fractionation during primary cracking of natural gas: a reaction kinetic approach. *Chemical Geology* **149**: 235-250.

Eiler J. M. and Schauble E. (2004) $^{18}O^{13}C^{16}O$ in Earth's atmosphere. *Geochimica et Cosmochimica Acta* **68**(23): 4767-4777.

Eren A. M., Morrison H. G., Lescault P. J., Reveillaud J., Vineis J. H. and Sogin M. L. (2015) Minimum entropy decomposition: Unsupervised oligotyping for sensitive partitioning of high-throughput marker gene sequences. *The ISME Journal* **9**: 968-979.

Etiope G. and Ionescu A. (2015) Low-temperature catalytic CO_2 hydrogenation with geological quantities of ruthenium: a possible abotic CH_4 source in chromitite-rich serpentinized rocks. *Geofluids* **15**: 438-452.

Etiope G. and Schoell M. (2014) Abiotic gas: atypical, but not rare. *Elements* **10**: 291-296.

Etiope G., Schoell M. and Hosgormez H. (2011) Abiotic methane flux from the Chimaera seep and Tekirova ophiolites (Turkey): understanding gas exhalation from low temperature serpentinization and implications for Mars. *Earth and Planetary Science Letters* **310**: 96-104.

Etiope G. and Sherwood Lollar B. (2013) Abiotic Methane on Earth. *Reviews of Geophysics* **51**: 276-299.

Etiope G., Vadillo I., Whiticar M. J., Marques J. M., Carreira P. M., Tiago I., Benavente J., Jimenez P. and Urresti B. (2016) Abiotic methane seepage in the Ronda peridotite massif, southern Spain. *Applied Geochemistry* **66**: 101-113.

Etiope G., Vance S., Christensen L. E., Marques J. M. and Ribeiro da Costa I. (2013) Methane in serpentinized ultramafic rocks in mainland Portugal. *Marine and Petroleum Geology* **45**: 12-16.

Foustoukos D. I. and Mysen B. O. (2013) H/D methane isotopologues dissolved in magmatic fluids: Stable hydrogen isotope fractionations in the Earth's interior. *American Mineralogist* **98**: 946-954.

Foustoukos D. I. and Seyfried W. E. J. (2004) Hydrocarbons in hydrothermal vent fluids: the role of chromium-bearing catalysts. *Science* **304**: 1002-1005.

Frantz J. D., Popp R. K. and Hoering T. C. (1992) The compositional limits of fluid immiscibility in the system H_2O-NaCl-CO_2 as determined with the use of synthetic fluid inclusions in conjunction with mass spectrometry. *Chemical Geology* **98**(3-4): 237-255.

Fu Q., Sherwood Lollar B., Horita J., Lacrampe-Couloume G. and Seyfried W. E. (2007) Abiotic formation of hydrocarbons under hydrothermal conditions: Constraints from chemical and isotope data. *Geochemica et Cosmochimica Acta* **71**: 1982-1998.

Glasby G. P. (2006) Abiogenic origin of hydrocarbons: an historical overview. *Resource Geology* **56**: 85-98.

Haghnegahdar M., Schauble E. A. and Young E. D. (2015). Constructing an atmospheric methane budget using $^{13}CH_3D$ and CH_2D_2 in sources and sinks. American Geophysical Union, San Francisco, CA, 827431.

Holland G., Sherwood Lollar B., Li L., Lacrampe-Couloume G., Slater G. F. and Ballentine C. J. (2013) Deep fracture fluids isolated in the crust since the Precambrian era. *Nature* **497**: 357-362.

Horita J. and Berndt M. E. (1999) Abiogenic methane formation and isotopic fractionation under hydrothermal conditions. *Science* **285**: 1055-1057.

Huse S. M., Dethlefsen L., Huber J. A., Welch D. M., Relman D. A. and Sogin M. L. (2008) Exploring microbial diversity and taxonomy using SSU rRNA hypervariable tag sequencing. *PLOS Genetics* **4**(11): 31000255.

1210 Ilkisik O. M. (1995) Regional heat flow in western Anatolia using silica temperature
1211 estimates from thermal springs. *Tectonophysics* **244**: 175-184.
1212 Jenden P. D., Drazan D. J. and Kaplan I. R. (1993) Mixing of thermogenic natural gases
1213 in Northern Appalachian Basin. *AAPG Bulletin* **77**: 980-998.
1214 Kelley D. S., Karson J. A., Fruh-Green G. L., Yoerger D. R., Shank T. M., Butterfield D.
1215 A., Hayes J. M., Shrenk M. O., Olson E. J., Proskurowski G., Jakuba M., Bradley
1216 A., Larson B., Ludwig K., Glickson D., Buckman K., Bradley A. S., Brazelton W.
1217 J., Roe K., Elend M. J., Delacour A., Bernasconi S. M., Lilley M. D., Baross J. A.,
1218 Summons R. E. and Sylva S. P. (2005) A serpentinite-hosted ecosystem: the Lost
1219 City hydrothermal field. *Science* **307**: 1428-1434.
1220 Kieft T. L., McCuddy M., Onstott T. C., Davidson M., Lin L.-H., Mislowack B., Pratt L.,
1221 Boice E., Sherwood Lollar B., Lippmann-Pipke J., Pfiffner S. M., Phelps T. J.,
1222 Gihring T., Moser D. and Van Heerden A. (2005) Geochemically generated,
1223 energy-rich substrates and indigenous microorganisms in deep, ancient
1224 groundwater. *Geomicrobiology Journal* **22**: 325-335.
1225 Klinman J. P. (2003) Dynamic barriers and tunneling. New views of hydrogen transfer in
1226 enzyme reactions. *Pure and Applied Chemistry* **75**: 601-608.
1227 Krishtalik L. I. (2000) The mechanism of the proton transfer: an outline. *Biochimica et*
1228 *Biophysica Acta* **1458**: 6-27.
1229 Lehr J. H. and Keeley J. (2016). Alternative Energy and Shale Gas Encylopedia.
1230 Hoboken, New Jersey, John Wiley & Sons.
1231 Limbach H.-H., Lopez J. M. and Kohen A. (2006) Arrhenius curves of hydrogen
1232 transfers: tunnel effects, isotope effects and effects of pre-equilibria.
1233 *Philosophical Transactions of the Royal Society B* **361**: 1399-1415.
1234 Lin L.-H., Wang P.-L., Rumble III D., Lippmann-Pipke J., Boice E., Pratt L. M.,
1235 Sherwood Lollar B., Brodie E. L., Hazen T. C., Anderson G. L., DeSantis T. Z.,
1236 Moser D. P., Kershaw D. and Onstott T. C. (2006) Long-term sustainability of a
1237 high-energy, low-diversity crustal biome. *Science* **314**: 479-482.
1238 Lippmann J., Stute M., Torgersen T., Moser D. P., Hall J. A., Lin L., Borcsik M.,
1239 Bellamy R. E. S. and Onstott T. C. (2003) Dating ultra-deep mine waters with
1240 noble gases and ^{36}Cl, Witwatersrand Basin, South Africa. *Geochemica et*
1241 *Cosmochimica Acta* **67**: 4597-4619.
1242 Lippmann-Pipke J., Sherwood Lollar B., Niedermann S., Stroncik N. A., Naumann R.,
1243 van Heerden E. and Onstott T. C. (2011) Neon identifies two billion year old fluid
1244 component in Kaapvaal Craton. *Chemical Geology* **283**: 287-296.
1245 Liu Q. and Liu Y. (2016) Clumped-isotope signatures at equilibrium of CH_4, NH_3, H_2O,
1246 H_2S and SO_2. *Geochemica et Cosmochimica Acta* **175**: 252-270.
1247 Lockridge J. P. (1977). Beecher Island Field Yuma County, Colorado. Rocky Mountain
1248 Association of Geologists 1977 Symposium**:** 271-279.
1249 Ma Q., Wu S. and Tang Y. (2008) Formation and abundance of doubly-substituted
1250 methane isotopologues ($^{13}CH_3D$) in natural gas systems. *Geochemica et*
1251 *Cosmochimica Acta* **72**(22): 5446-5456.
1252 Magnabosca C., Timmers P. H. A., Lau M. C. Y., Borgonie G., Linage-Alvarez B.,
1253 Kuloyo O., Alleva R., Kieft T. L., Slater G. S., van Heerden E., Sherwood Lollar
1254 B. and Onstott T. C. (2016) "The case for a dynamical subsurface ecosystem."
1255 BioRxiv DOI: http://dx.doi.org/10.1101/040204.

McCollom T. M. and Seewald J. S. (2006) Carbon isotope composition of organic compounds produced by abiotic synthesis under hydrothermal conditions. *Earth and Planetary Science Letters* **243**: 74-84.
McCollom T. M. and Seewald J. S. (2007) Abiotic synthesis of organic compounds in deep-sea hydrothermal environments. *Chemical Reviews* **107**: 382-401.
McKinney C. R., McCrea J. M., Epstein S., Allen H. A. and Urey H. C. (1950) Improvements in mass spectrometers for the measurement of small differences in isotope abundance ratios. *The Review of Scientific Instruments* **21**(8): 724-730.
Omar G. I., Onstott T. C. and Hoek J. (2003) The origin of deep subsurface microbial communities in the Witwatersrand Basin, South Africa as deduced from apatite fission track analyses. *Geofluids* **3**: 69-80.
Ono S., Wang D. T., Gruen D. S., Sherwood Lollar B., Zahniser M. S., McManus B. J. and Nelson D. D. (2014) Measurement of a doubly substituted methane isotopologue, 13CH3D, by tunable infrared laser direct absorption spectroscopy. *Analytical Chemistry* **86**: 6487-6494.
Onstott T. C., Moser D. P., Pfiffner S. M., Fredrickson J. K., Brockman F. J., Phelps T. J., White D. C., Peacock A., Balkwill D., Hoover R., Krumholz L. R., Broscik M., Kieft T. L. and Wilson R. (2003) Indigenous and contaminant microbes in ultradeep mines. *Environmental Microbiology* **5**(11): 1168-1191.
Proskurowski G., Lilley M. D., Kelley D. S. and Olson E. J. (2006) Low temperature volatile production at the Lost City Hydrothermal Field, evidence from a hydrogen stable isotope geothermometer. *Chemical Geology* **229**: 331-343.
Proskurowski G., Lilley M. D., Seewald J. S., Fruh-Green G. L., Olsen E. J., Lupton J. E., Sylva S. P. and Kelley D. S. (2008) Abiogenic hydrocarbon production at Lost City Hydrothermal Field. *Science* **319**: 604-607.
Proskurowski G., Lilley M. D., Seewald J. S., Fruh-Green G. L., Olson E. J., Lupton J. E., Sylva S. P. and Kelley D. S. (2008) Abiogenic hydrocarbon production in Lost City hydorthermal field. *Science* **319**: 604-607.
Qi Y., Yang J., Duan X., Zhu Y.-A., Chen D. and Holmen A. (2014) Discrimination of the mechanism of CH4 formation in Fischer-Tropsch synthesis on Co catalysts: a combined approach of DFT, kinetic isotope effects and kinetic analysis. *Catalysis Science & Technology* **4**: 3534-3542.
Rockmann T., Popa M. E., Krol M. C. and Hofmann M. E. G. (2016) Statistical clumped isotope signatures. *Scientific Reports*: (in press).
Rowan E. (2006). Burial and Thermal History of the Central Appalachian Basin, Based on three 2-D Models of Ohio, Pennsylvania, and West Virginia. U. S. D. o. t. Interior. Geological Survey Open File Report 2006-1019.
Scheller S., Goenrich M., Boecher R., Thauer R. K. and Juan B. (2010) The key nickel enzyme of methanogenesis catalyses the anaerobic oxidation of methane. *Nature* **465**: 606-609.
Schoell M. (1988) Multiple origins of methane in the Earth. *Chemical Geology* **71**: 1-10.
Schrenk M. O., Brazelton W. J. and Lang S. Q. (2013). Serpentinization, Carbon, and Deep Life. Reviews in Mineralogy & Geochemistry, Carbon in Earth. R. M. Hazen, A. P. Jones and J. A. Baross. Chantilly, Mineralogical Society of America. **75:** 575-606.

1301 Schuiling R. D. (1964) Serpentinization as a possible cause of high heat-flow values in
1302 and near the oceanic ridges. *Nature* **201**: 807-808.
1303 Sessions A. L., Sylva S. P., Summons R. E. and Hayes J. M. (2004) Isotopic exchange of
1304 carbon-bound hydrogen over geologic timescales. *Geochemica et Cosmochimica*
1305 *Acta* **68**(7): 1545-1559.
1306 Sherwood Lollar B., Lacrampe-Couloume G., Slater G. F., Ward J., Moser D. P., Gihring
1307 T. M., Lin L.-H. and Onstott T. C. (2006) Unravelling abiogenic and biogenic
1308 sources of methane in the Earth's deep subsurface. *Chemical Geology* **226**: 328-
1309 339.
1310 Sherwood Lollar B., Lacrampe-Couloume G., Voglesonger K., Onstott T. C., Pratt L. M.
1311 and Slater G. F. (2008) Isotopic signatures of CH4 and higher hydrocarbon gases
1312 from Precambrian Shield sites: A model for abiogenic plymerization of
1313 hydrocarbons. *Geochemica et Cosmochimica Acta* **72**: 4778-4795.
1314 Sherwood Lollar B., Onstott T. C., Lacrampe-Couloume G. and Ballentine C. J. (2014)
1315 The contribution of the Precambrian continental lithosphere to global H_2
1316 production. *Nature* **14017**: 379-382.
1317 Sherwood Lollar B., Voglesonger K., Lin L.-H., Lacrampe-Couloume G., Telling J.,
1318 Abrajano T. A., Onstott T. C. and Pratt L. M. (2007) Hydrogeologic controls on
1319 episodic H_2 release from Precambrian fractured rocks - energy for deep
1320 subsurface life on Earth and Mars. *Astrobiology* **7**(6): 971-986.
1321 Sherwood Lollar B., Westgate T. D., Ward J. A., Slater G. F. and Lacrampe-Couloume G.
1322 (2002) Abogenic formation of gaseous alkanes in the Earth's crust as a minor
1323 source of global hydrocarbon reservoirs. *Nature* **416**: 522-524.
1324 Simkus D. N., Slater G. F., Sherwood Lollar B., Wilkie K., Kieft T. L., Magnabosca C.,
1325 Lau M. C. Y., Pullin M. J., Hendrickson S. B., Wommack K. E., Sakowski E. G.,
1326 van Heerden E., Kuloyo O., Linage B., Borgonie G. and Onstott T. C. (2016)
1327 Variations in microbial carbon sources and cycling in the deep continental
1328 subsurface. *Geochemica et Cosmochimica Acta* **173**: 264-283.
1329 Stolper D. A., Lawson M., Davis C. L., Ferreira A. A., Santos Neto E. V., Ellis G. S.,
1330 Lewan M. D., Martini A. M., Tang Y., Schoell M., Sessions A. L. and Eiler J. M.
1331 (2014) Formation temperatures of thermogenic and biogenic methane. *Science*
1332 **344**: 1500-1503.
1333 Stolper D. A., Martini A. M., Clog M., Douglas P. M., Shusta S. S., Valentine D. L.,
1334 Sessions A. L. and Eiler J. M. (2015) Distinguishing and understanding
1335 thermogenic and biogenic sources of methane using multiply substituted
1336 isotopologues. *Geochemica et Cosmochimica Acta* **161**: 219-247.
1337 Stolper D. A., Sessions A. L., Ferreira A. A., Santos Neto E. V., Schimmelmann A.,
1338 Shusta S. S., Valentine D. L. and Eiler J. M. (2014) Combined 13C-D and D-D
1339 clumping in methane: Methods and preliminary results. *Geochemica et*
1340 *Cosmochimica Acta* **126**: 169-191.
1341 Takai K., Nakamura K., Toki T., Tsunogai U., Miyazaki M., Miyazaki J., Hirayama H.,
1342 Nakagawa S., Nunoura T. and Horikoshi K. (2008) Cell proliferation at 122
1343 degrees C and isotopically heavy CH_4 production by hyperthermophiic
1344 methanogen under high-pressure cultivation. *Proceedings of the National*
1345 *Academy of Sciences* **105**: 10949-10954.

Tang Y., Perry J. K., Jenden P. D. and Schoell M. (2000) Mathematical modeling of stable carbon isotope ratios in natural gases. *Geochemica et Cosmochimica Acta* **64**: 2673-2687.

Tuttle O. F. (1949) Two pressure vessels for silicate-water studies. *Geological Society of America Bulletin* **60**(10): 1727-1729.

Valentine D. L. (2011) Emerging topics in marine methane biogeochemistry. *Annual Review of Marine Science* **3**: 147-171.

Wang D. T., Gruen D. S., Sherwood Lollar B., Hinrichs K.-U., Stewart L. C., Holden J. F., Hristov A. N., Pohlman J. W., Morrill P. L., Könneke M., Delwiche K. B., Reeves E. P., Sutcliffe C. N., Ritter D. J., Seewald J. S., McIntosh J. C., Hemond H. F., Kubo M. D., Cardace D., Hoehler T. M. and Ono S. (2015) Nonequilibrium clumped isotope signals in microbial methane. *Science* **348**: 428-431.

Wang W., Wang S., Ma X. and gong J. (2011) Recent advances in catalytic hydorgenation of carbon dioxide. *Chemical Society Reviews* **40**: 3703-3727.

Ward J. A., Slater G. F., Moser D. P., Lin L.-H., Lacrampe-Couloume G., Bonn A. S., Davidson M., Hall J. A., Mislowack B., Bellamy R. E. S., Onstott T. C. and Sherwood Lollar B. (2004) Microbial hydrocarbon gases in the Witwatersrand Basin, South Africa: Implications for the deep biosphere. *Geochemica et Cosmochimica Acta* **68**: 3239-3250.

Webb M. A. and Miller T. F., III (2014) Position-specific and clumped stable isotope studies: comparison of the Urey and path-integral appraoches for carbon dioxide, methane, and propane. *The Journal of Physical Chemistry* **118**: 467-474.

Webster C. R., Mahaffy P. R., Atreya S. K., Flesch G. J., Mischna M. A., Meslin P., Farley K. A., Conrad P. G., Christensen L. E., Pavlov A. A., Martin-Torres J., Zorzano M.-P., McConnochie T. H., Owen T., Eigenbrode J. L., Glavin D. P., Steele A., Malespin C. A., Archer Jr. P. D., Sutter B., Coll P., Freissinet C., McKay C. P., Moores J. E., Schwenzer S. P., Bridges J. C., Navarro-Gonzalez R., Gellert R., Lemmon M. T. and Team M. S. (2015) Mars methane detection and variability at Gale crater. *Science* **347**: 415-417.

Whiticar M. J. and Etiope G. (2014). Methane in land-based serpentinization peridotites: new discoveries and isotope surprises. American Geophysical Union, San Francisco,

Wongnate T., Sliwa D., Ginovska B., Smith D., Wolf M. W., Lehnert N., Raugei S. and Ragsdale W. (2016) The radical mechanism of biological methane synthesis by methyl-coenzyme M reductase. *Science* **352**(6288): 953-959.

Yeung L. Y. (2016) Combinatorial effects on clumped isotopes and their significance in biogeochemistry. *Geochemica et Cosmochimica Acta* **172**: 22-38.

Young E. D., Rumble III D., Freedman P. and Mills M. (2016) A large-radius high-mass-resolution multiple-collector isotope ratio mass spectrometer for analysis of rare isotopologues of O_2, N_2, CH_4 and other gases. *International Journal of Mass Spectrometry* **401**: 1-10.

Young E. D., Rumble III D., Freedman P., Schauble E. and guo W. (2011) Invited: high mass resolution gas-source mass spectrometry. *Mineralogical Magazine* **73**: 2229.

Ysohinaga M. Y., Holler T., Goldhammer T., Wegener G., Phlman J. W., Brunner B., Kuypers M. M. M., Hinrichs K.-U. and Elvert M. (2014) Carbon isotope

equilibration during sulphate-limited anearobic oxidation of methane. *Nature Geoscience* **7**: 190-195.

Yu Y., Yang J., Hao C., Zhao X. and Wang Z. (2009) The adsorption, vibration and diffusion of hydrogen atoms on platinum low-index surfaces. *Journal of Computational and Theoretical Nanoscience* **6**: 439-448.

Table 1

Table 1. Isotope ratio data for CH_4 collected as part of this study together with isotope ratio data for coexisting H_2 and H_2O and calculated inter-species temperatures. All delta values and their uncertainties are given in ‰.

	Days since hole drilled	$\delta^{13}C$ CH_4 (VPDB)	±1se	δD CH_4 (VSMOW)	±1se	$\Delta^{13}CH_3D$	±1se	ΔCH_2D_2	±1se	Vol % H_2	δD H_2 (VSMOW)	δD H_2O (VSMOW)	CH_4/H_2 T°C, Horibe & Craig (1999)	CH_4/H_2 T°C, Bottinga (1969)	H_2OL/H_2 T°C, Horibe & Craig (1999)
Canadian Shield															
Kidd Creek 7850 12287A 19.09.2013	2334	-41.404	0.004	-389.52	0.02	5.34	0.11	14.86	0.29	5.74	-739	-35.68	83.91	114	30
Kidd Creek 7850 12299 02.04.2014	2500	-39.644	0.003	-391.46	0.02	5.75	0.10	17.98	0.27	2.62	-736	-34.42	88.20	118	33
Kidd Creek 7850 12261 22.10.2015	3087	-38.735	0.013	-411.67	0.02	5.81	0.08	16.39	0.30	3.07		-33.43			
Kidd Creek 7850 12287A 02.04.2014	2529	-41.858	0.003	-391.54	0.02	5.03	0.12	14.03	0.32	3.69	-734		90.48	121	
Kidd Creek 9500 13762 14.06.2012	99	-32.598	0.003	-422.25	0.02	5.58	0.08	-6.27	0.25	17.08	-717	-29.31	127.73	160	44
Kidd Creek 9500 13684 14.06.2012	177	-32.147	0.014	-429.34	0.01	5.76	0.09	-9.91	0.24	12.15	-717	-30.89	132.20	165	44
Kidd Creek 9500 13762 16.01.2013	315	-35.919	0.016	-421.25	0.02	6.00	0.07	5.25	0.29	0.34	-714	-77.28	130.91	164	56
Kidd Creek 9500 BH2 28.11.2012	334	-32.709	0.005	-420.75	0.02	5.19	0.13	-6.34	0.31	15.24	-708		138.27	172	
Kidd Creek 9500 13762 16.01.2013 (2)	315	-34.300	0.005	-419.85	0.02	5.37	0.11	4.05	0.33	0.34	-714		130.03	163	
Kidd Creek 9500 BH2 16.01.2013	381	-31.787	0.004	-420.01	0.02	5.26	0.12	-8.45	0.31	15.57	-714	-28.37	130.13	163	45
Birchtree 3900 9167 06.11.2007		-49.736	0.012	-343.93	0.01	6.05	0.17	21.61	0.29						
Witwatersrand Basin															
Masimong MM51940FW 29.06.2012		-58.921	0.003	-216.60	0.04	6.10	0.15	13.58	0.47	0.01		-40.06			
Beatrix BE326FW 07.12.2011		-53.512	0.024	-206.39	0.02	6.49	0.12	13.90	0.44	0.01		-41.36			
Kloof KL445FW 19.07.2011		-36.167	0.015	-323.67	0.02	3.13	0.11	15.43	0.33	0.01		-30.34			
Tau Tona 109FW 08.02.2012		-41.096	0.007	-367.06	0.02	5.14	0.10	2.98	0.39	0.01		-25.29			
Tau Tona 107FW 08.11.2011		-41.932	0.007	-359.77	0.02	4.95	0.09	4.25	0.32	0.01					
On-shore ultramafic complexes															
Chimaera G1		-12.644	0.003	-121.07	0.02	3.59	0.13	8.45	0.65		-720¶		13.12	43	
Chimaera G2		-14.630	0.003	-122.25	0.01	3.26	0.11	10.24	0.42		-720¶		13.39	43	
Chimaera G3		-12.493	0.004	-120.83	0.01	3.49	0.13	9.02	0.38		-720¶		13.07	43	
Cabeco de Vide		-23.977	0.010	-282.63	0.06	3.32	0.01	-7.57	0.34						
Acqusasanta Terme	3500	-9.477	0.005	-251.56	0.02	1.86	0.01	15.80	0.34						
Thermogenic gases															
Beecher Island field, Denver Basin		-61.572	0.035	-219.82	0.01	3.23	0.12	5.51	0.41						
Marcellus Shale		-36.449	0.005	-158.31	0.01	3.11	0.09	9.33	0.44						

Utica Shale	-25.969	0.007	-154.00	0.02	3.05	0.12	9.25	0.41	
Methanogenic CH4 in the laboratory									
Methanosarcina acetivorans, 30°C	-32.768	0.007	-328.41	0.02	-3.88	0.20	-40.86	0.36	
Methanosarcina acetivorans, 30°C	-32.763	0.005	-328.45	0.02	-3.84	0.09	-43.24	0.31	
Methanosarcina barkeri, 30°C	-56.550	0.007	-340.18	0.02	-1.11	0.13	-34.33	0.35	
Methanococcus thermolithotrophicus , 65°C	-49.355	0.011	-394.37	0.02	2.66	0.10	-19.44	0.30	
Abitoic CH4 in the laboratory									
Sabatier reaction, 90°C	-37.393	0.000	-434.02	0.29	4.20	0.52	-55.86	2.01	
Sabatier reaction, 70°C	-43.095	0.012	-417.80	0.04	3.08	0.17	-53.69	0.54	
$Si_5C_{12}H_{36}+H_2O$ 600°C	-48.567	0.007	-134.41	0.02	0.62	0.14	1.41	0.50	
$Si_5C_{12}H_{36}+H_2O$ 600°C	-48.548	0.011	-155.72	0.02	0.52	0.22	0.37	0.46	
$Si_5C_{12}H_{36}+H_2O$ 600°C, not catalyzed	-49.772	0.009	-157.06	0.01	0.04	0.12	0.74	0.40	
$Si_5C_{12}H_{36}+H_2O$ 500°C	-50.657	0.004	-230.27	0.02	-0.18	0.11	-4.79	0.409	
$Si_5C_{12}H_{36}+H_2O$ 500°C	-53.882	0.014	-271.80	0.02	0.74	0.16	-9.20	0.45	
$Si_5C_{12}H_{36}+H_2O$ 400°C	-49.197	0.004	-185.75	0.02	0.30	0.13	-2.28	0.47	
$Si_5C_{12}H_{36}+H_2O$ 400°C, not catalyzed	-49.063	0.012	-246.19	0.01	1.08	0.15	-3.04	0.34	
$Si_5C_{12}H_{36}+H_2O$ 300°C	-51.205	0.008	-248.85	0.01	0.50	0.14	-7.64	0.39	
Equilibration on Pt									
UCLA1 500C +/-5 °C	-40.401	0.003	-79.41	0.02	0.74	0.14	1.81	0.50	
UCLA1 300+/-10 °C	-37.013	0.005	-106.90	0.01	1.70	0.16	3.17	0.43	
UCLA1 400C +/-5 °C	-37.353	0.003	-86.60	0.02	1.28	0.10	1.94	0.46	
UCLA1 500C +/-5 °C	-37.767	0.010	-69.16	0.02	0.99	0.12	0.96	0.55	
UCLA1 400C +/-5 °C	-37.099	0.003	-93.81	0.01	1.10	0.11	2.04	0.46	

[¶]Etiope et al. (2011).

Figures and captions

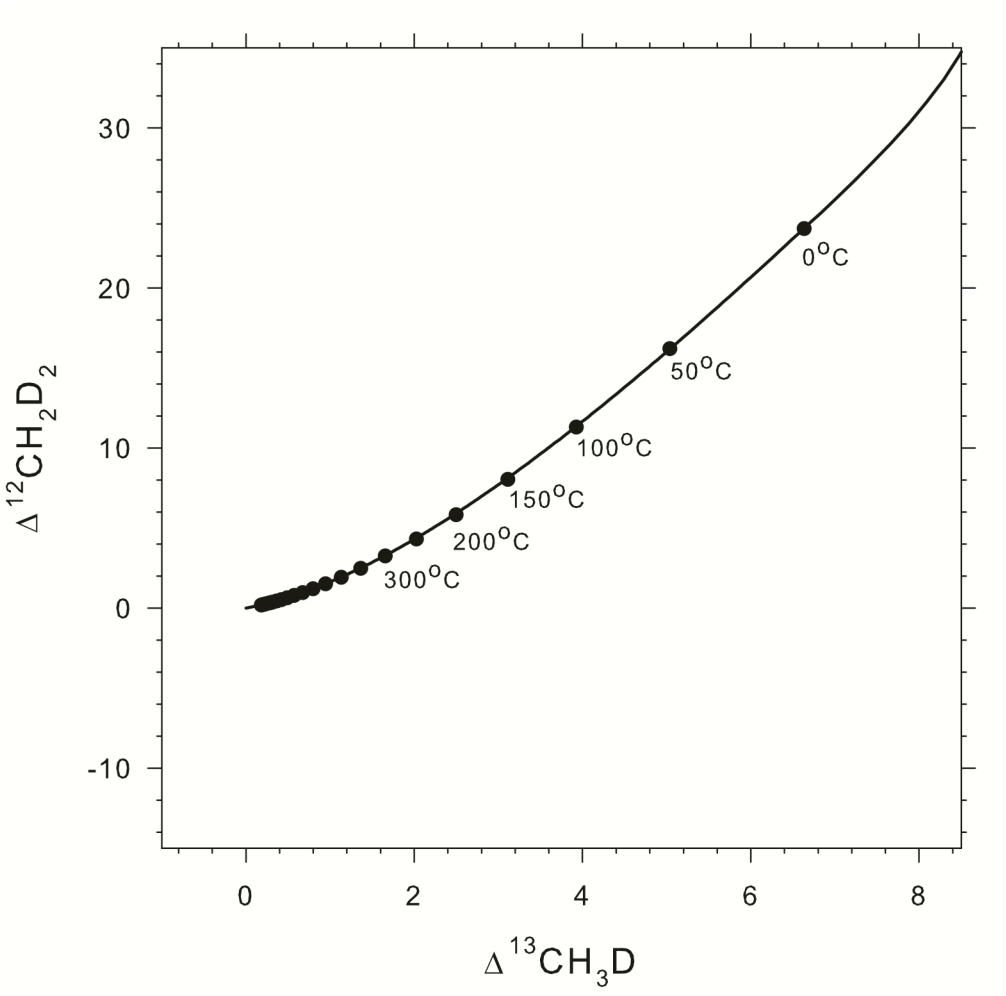

Figure 1. Thermodynamic equilibrium curve in $\Delta^{12}CH_2D_2$ vs. $\Delta^{13}CH_3D$ space. Both axes are in per mil.

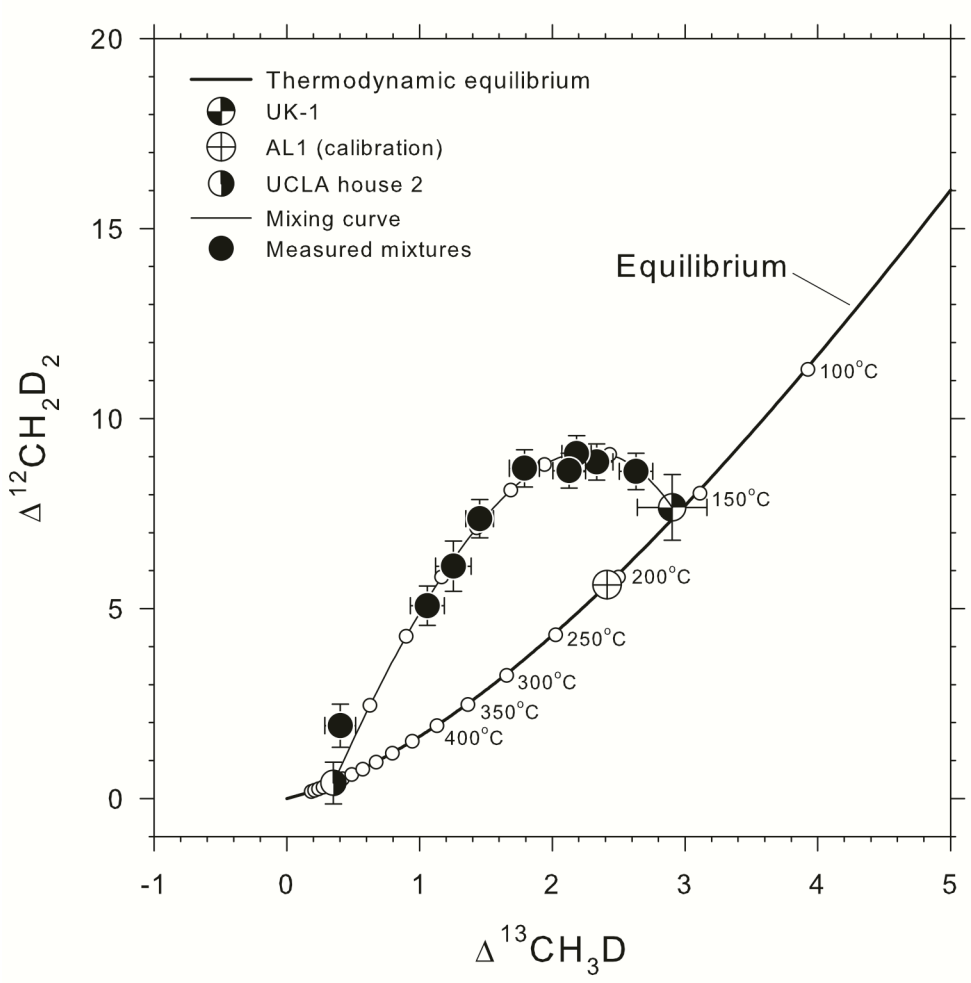

Figure 2. Measured mixtures (black symbols) of two gases performed in the laboratory at UCLA (Young et al. 2016). The predicted mixing curve is shown with the thin curve and white points marking 10% intervals of mixing. Reproduced from Fig. 12 of Young et al. (2016). Both axes are in per mil.

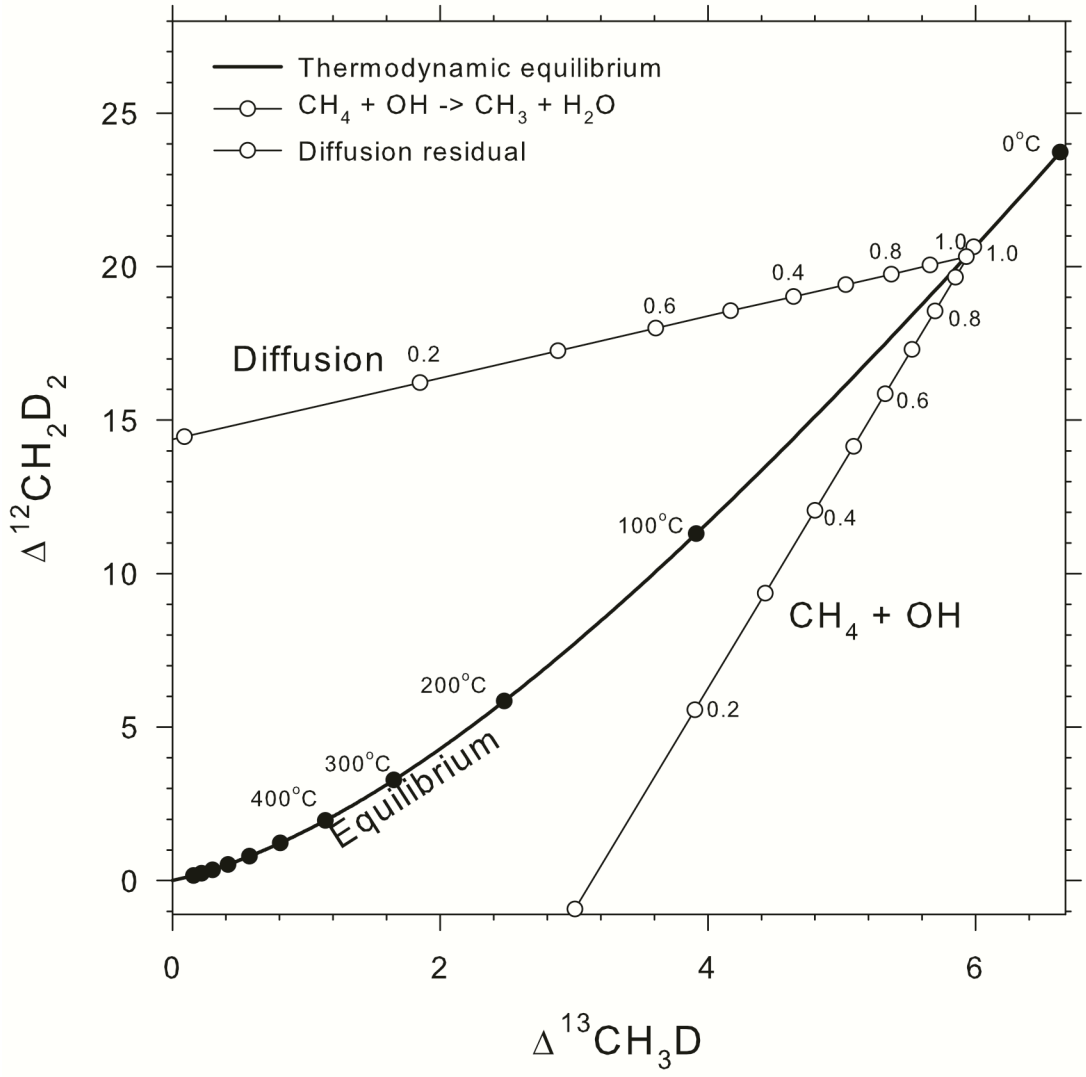

Figure 3. Comparison of the effects of diffusion and reaction kinetics with thermodynamic equilibrium in ΔCH_2D_2 vs. $\Delta^{13}CH_3D$ space. Numbers along trend lines refer to fractions of original gas remaining after Rayleigh fractionation. CH_4 + OH kinetics are from Haghnegahdar et al. (2015).

Figure 4. The locations of methane samples analyzed as part of this survey (Google Earth).

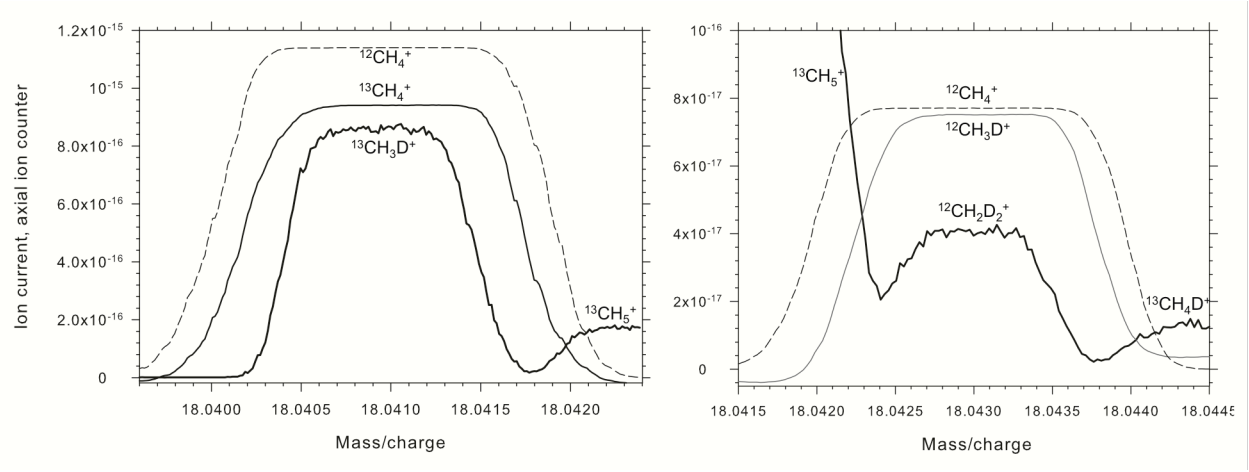

Figure 5. Mass spectrometry peak shapes for methane gas obtained using the analytical methods used in this study. Left: magnet current and collector slit settings for analysis of $\delta^{13}C$ and $\Delta^{13}CH_3D$. Right: settings for analysis of δD and $\Delta^{12}CH_2D_2$. The ordinate values are ion currents for the axial ion counter in amps. The abscissa units are daltons/unit charge (thomsons). Ion counter peak shapes are averages of 20 individual scans. Mass-17 and mass-16 peaks are scaled for direct comparison with the axial mass-18 beam currents.

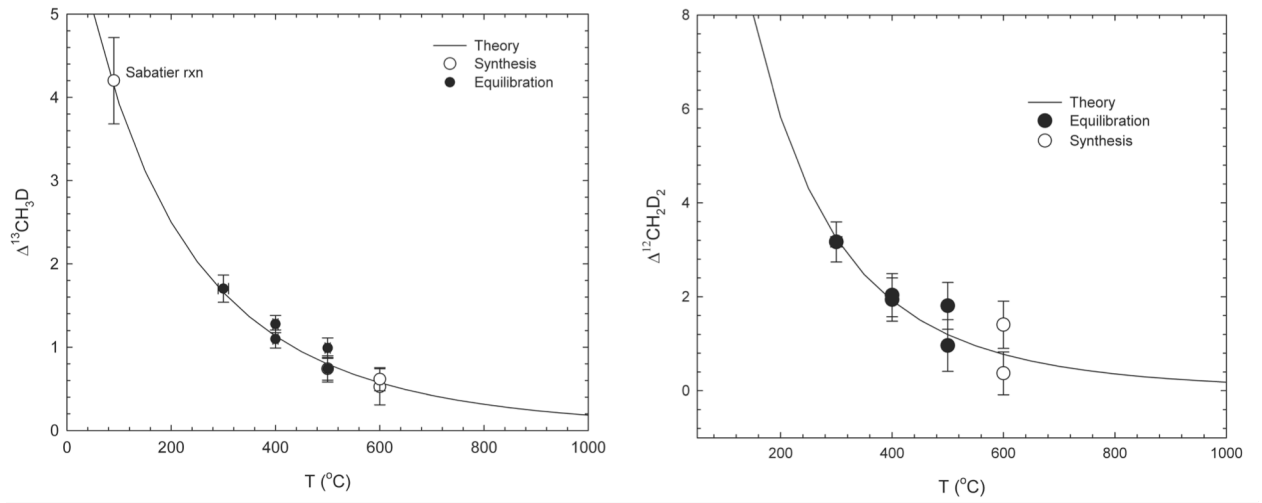

Figure 6. Plots of catalyzed CH_4 intra-species isotope exchange experiments (black symbols) and high-temperature CH_4 abiotic synthesis experiments (open symbols) compared with the theoretical relationships between $\Delta^{13}CH_3D$ vs. T (left) and $\Delta^{12}CH_2D_2$ vs. T (right).

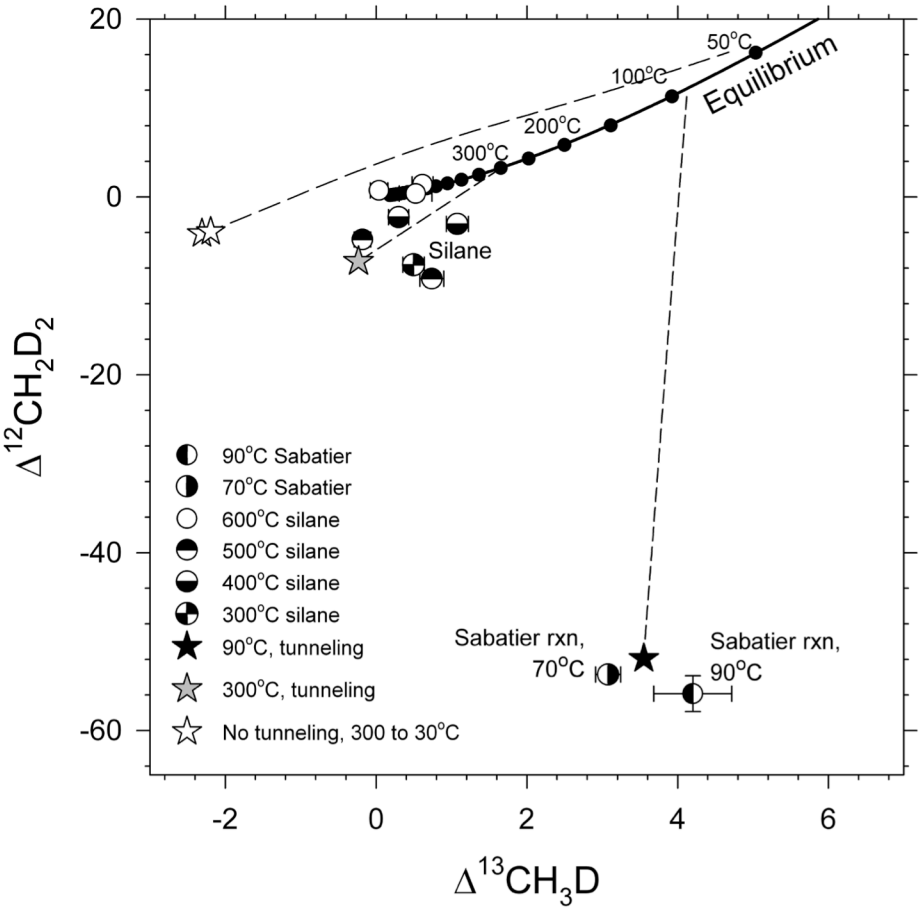

Figure 7. Plot of $\Delta^{12}CH_2D_2$ and $\Delta^{13}CH_3D$ values for methane gases produced abiotically in the laboratory by the Sabatier reaction and the hydrolysis of silane. Also shown are results of kinetic models for the isotopic effects of metal-catalyzed abiotic methane formation described in the text. Open stars show the results of classical kinetics. The black (90°C) and grey (300°C) stars show the results that include quantum tunneling. Dashed lines show the calculated evolution paths towards equilibrium for each kinetic model. The equilibrium curve is shown for reference.

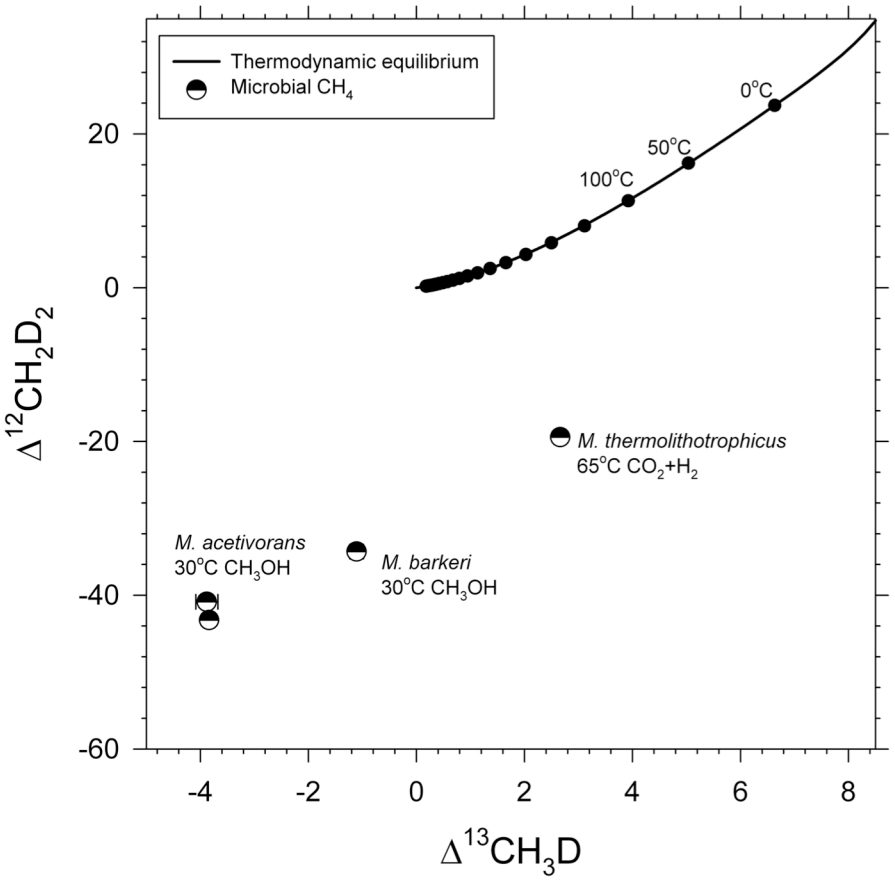

Figure 8. $\Delta^{12}CH_2D_2$ vs. $\Delta^{13}CH_3D$ plot comparing the methane produced in the laboratory by three methanogen species of methanogenic Archaea. The equilibrium curve is shown for reference.

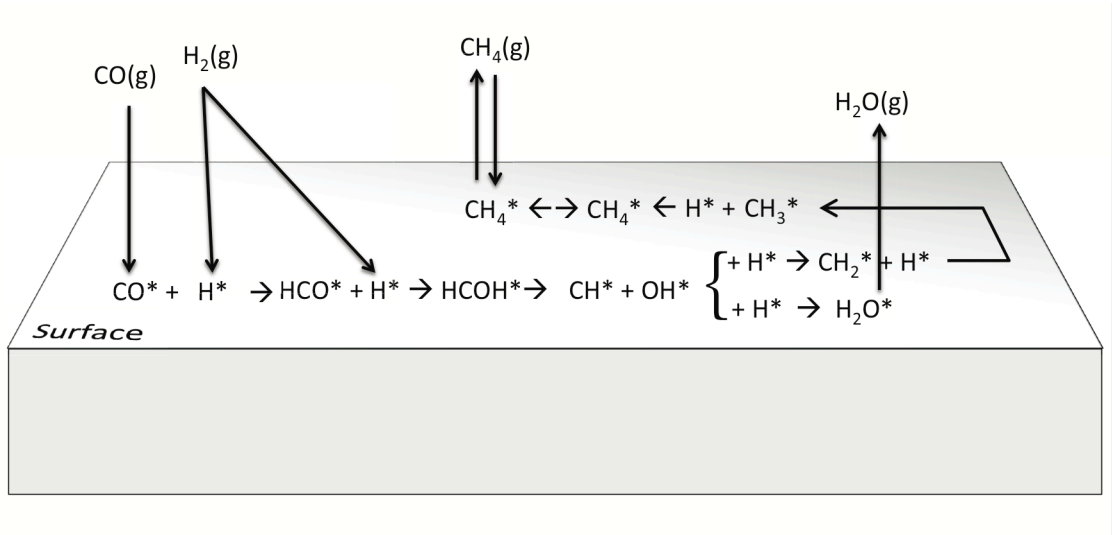

Figure 9. Schematic showing the reaction scheme used to model the production of methane from CO and H_2 gases catalyzed on a metal surface.

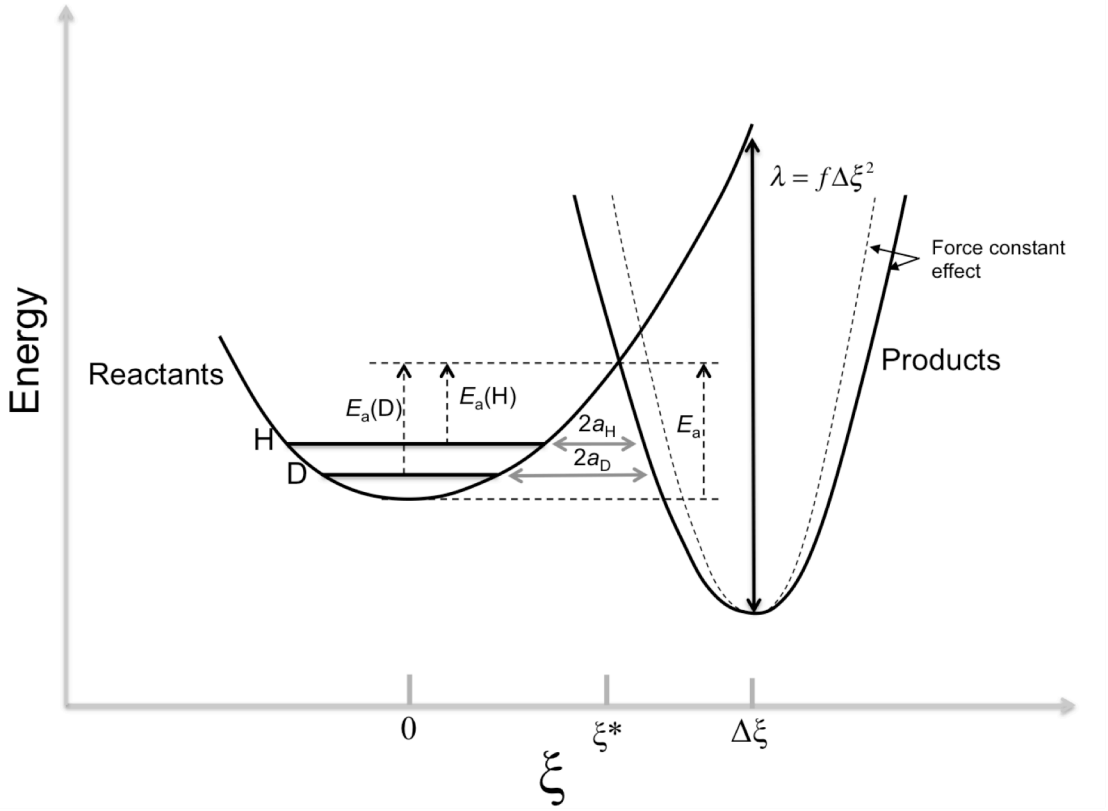

Figure 10. Schematic illustrating the relationships between activation energy, E_a, tunneling distances for hydrogen (a_H) and deuterium (a_D) and the non-adiabatic energy parabolas representing adsorbed reactants and product. The ordinate is potential energy. The abscissa is the reaction progress coordinate ξ. Differences in tunneling distances are seen to imply corresponding differences in activation barriers for insertion of H and D atoms $E_a(H)$ and $E_a(D)$, respectively. $\Delta\xi$ is the separation between reactant and product energy minima that together with force constant f, controls the reorganization energy λ in the context of Marcus theory. ξ^* is the reaction coordinate position of the energy barrier for the reaction.

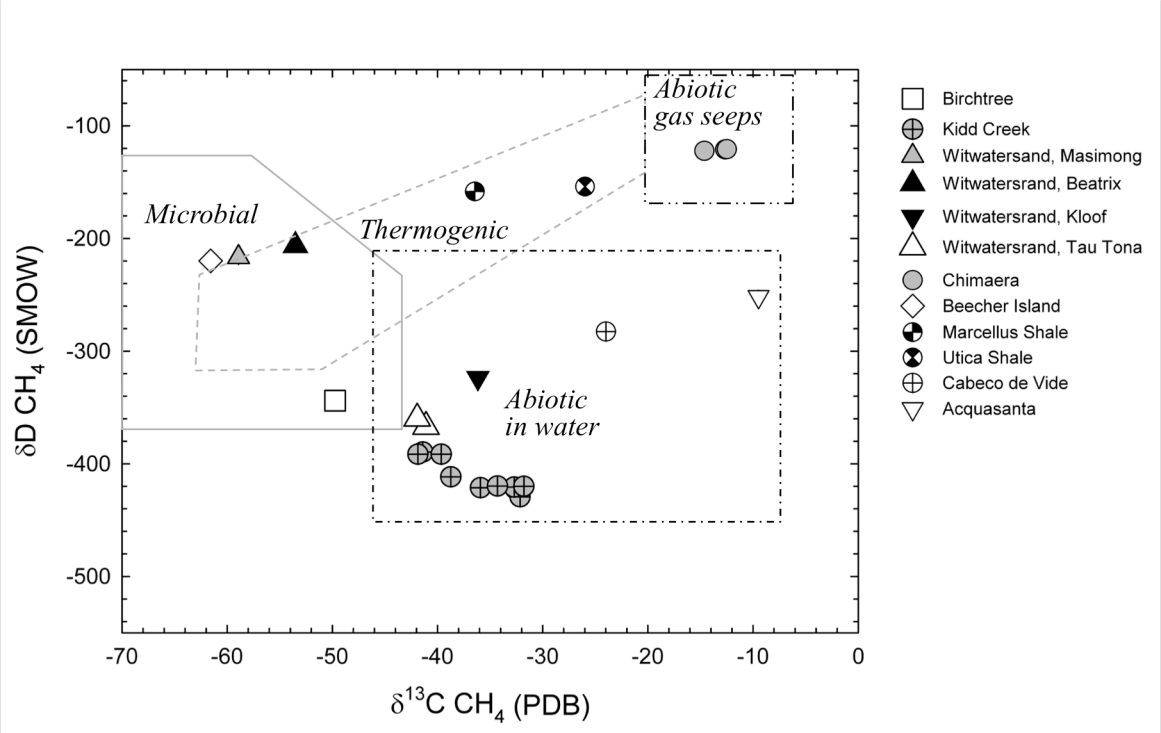

Figure 11. δD (VSMOW) and $\delta^{13}C$ (VPDB) of gases used in this study. Nominal fields for microbial, thermogenic and abiotic gas based are also shown for reference and are based on previously published literature compilations (e.g., Etiope and Sherwood Lollar, 2013, and references therein). Abiotic gases are further divided into two fields, those gases dissolved in waters and those issuing from gas seeps.

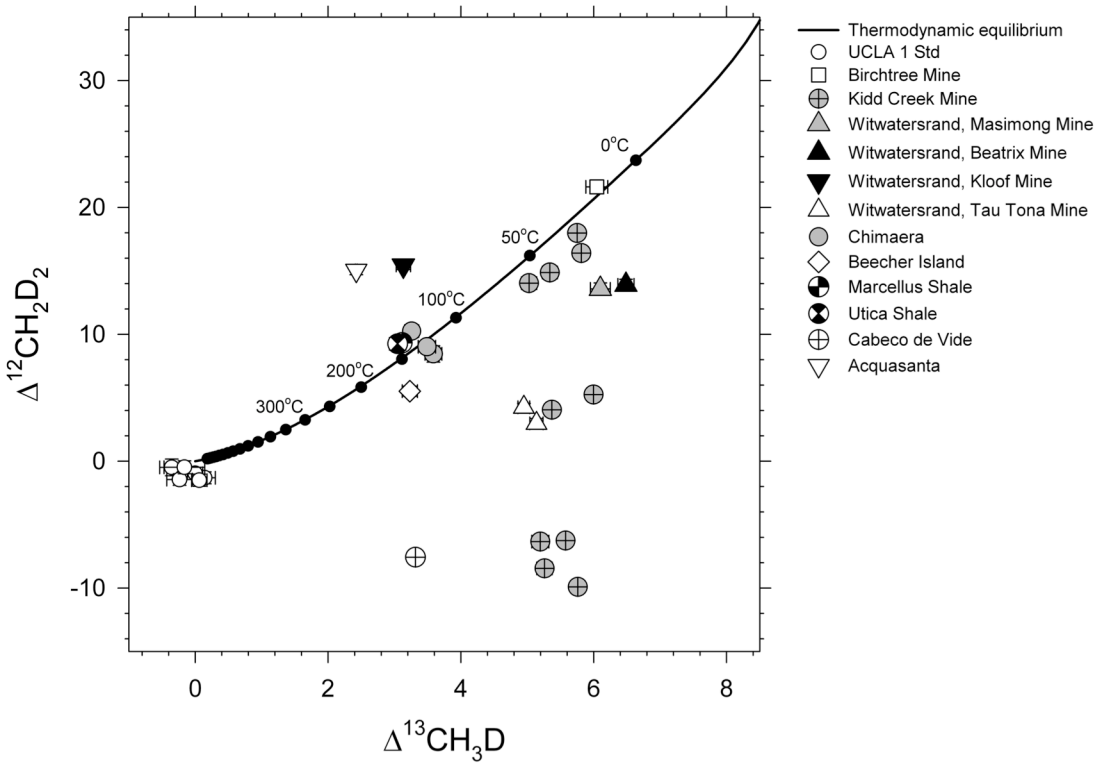

Figure 12. $\Delta^{12}CH_2D_2$ vs $\Delta^{13}CH_3D$ for all natural samples in this study. The curve denoting thermodynamic equilibrium is shown for reference. Also shown are replicates of an in-house standard, UCLA-1, as an illustration of external precision.

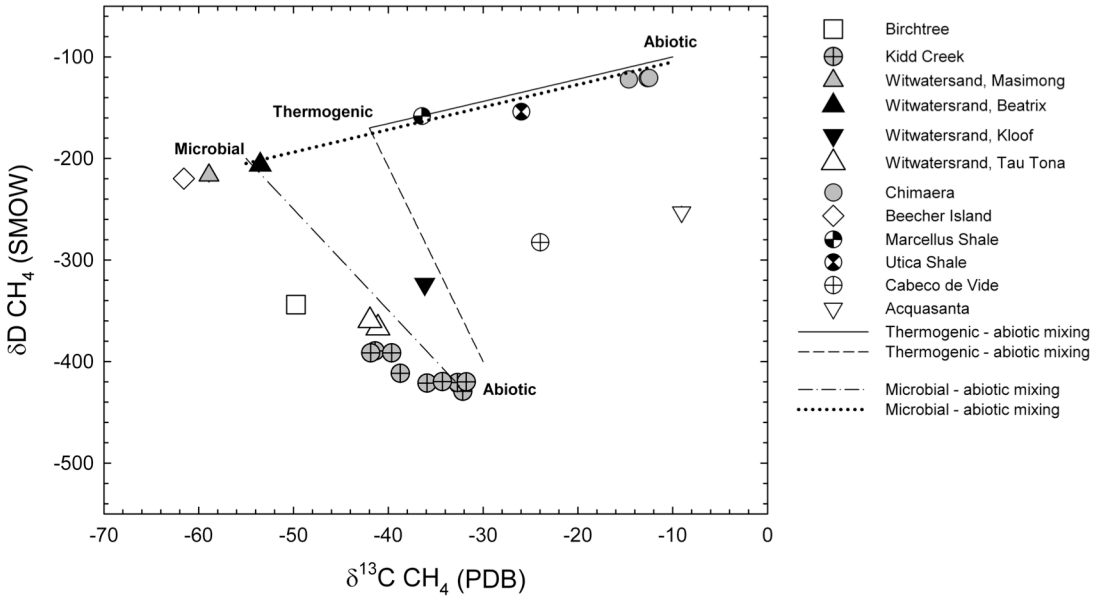

Figure 13. Mixing scenarios discussed in the text in δD (SMOW) vs. δ^{13}C (PDB) space.

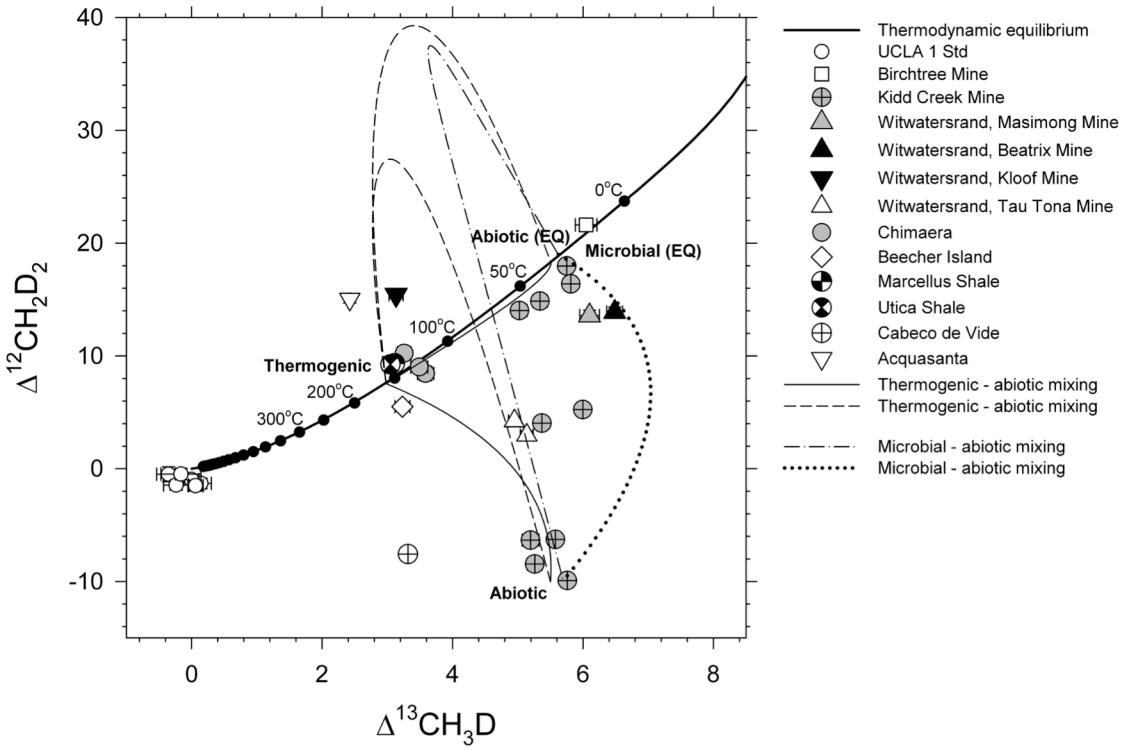

Figure 14. Mixing scenarios discussed in the text in $\Delta^{12}CH_2D_2$ vs. $\Delta^{13}CH_3D$ space. Some of the endmember compositions discussed in the text are labeled. Abiotic (EQ) and Microbial (EQ) refer to methane gases produced by abiotic reactions or by microbial activity that have equilibrium isotope bond ordering. Two dashed curves depicting mixing between a thermogenic component on the equilibrium curve and two different abiotic endmember compositions, one in thermodynamic equilibrium and the other not, are shown. The compositions of the endmembers are indicated by the terminal points on each curve.

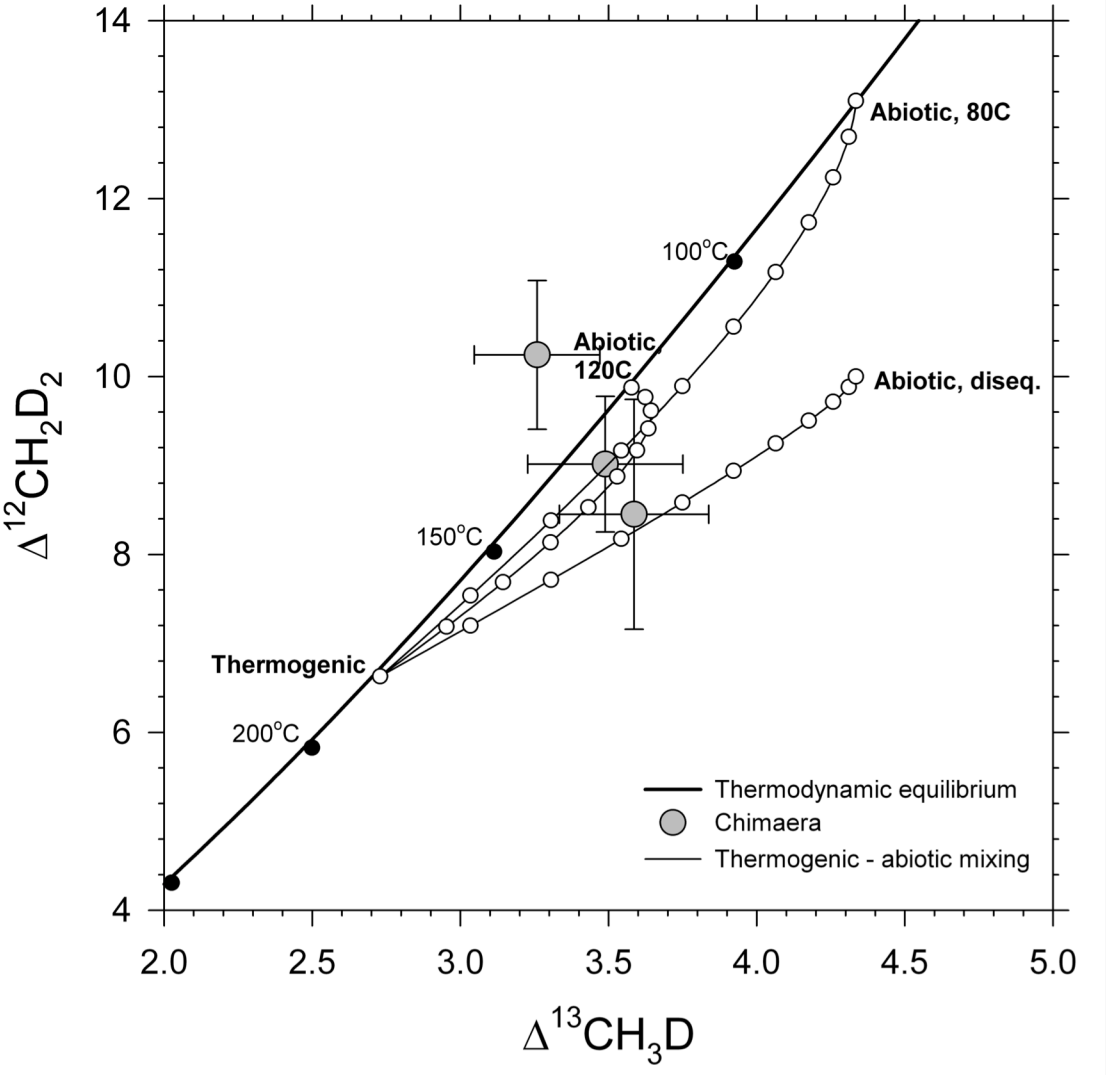

Figure 15. Mixing scenarios discussed in the text in $\Delta^{12}CH_2D_2$ vs. $\Delta^{13}CH_3D$ space specific to the Chimaera CH_4 gas. Various possible abiotic endmember compositions are shown, including equilibrated gases at 80°C and 120°C and a disequilibrium component, mixed with a thermogenic gas formed at 180°C. The thin solid lines correspond to the mixing path in δD vs $\delta^{13}C$ space shown with the same line solid line symbol in Figure 13. White circles mark 10% intervals of mixing ratios for each of the three mixing curves. The error bars for the Chimaera data represent 2 se (internal errors) in this figure. The thermodynamic equilibrium curve is shown as the heavy line with black dots for reference.

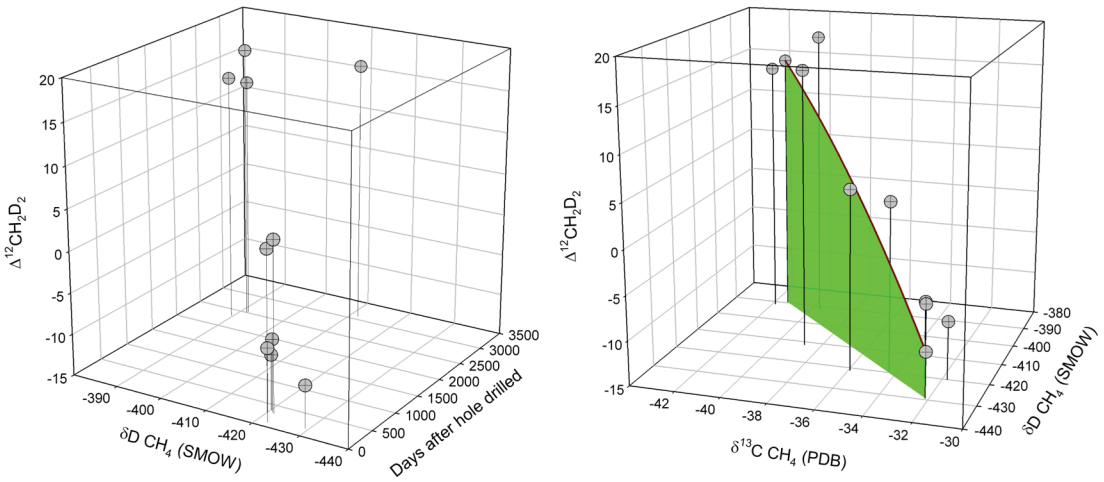

Figure 16. Plots of methane δD and $\Delta^{12}CH_2D_2$ versus days since borehole at Kidd Creek was drilled (left) and δD, $\Delta^{12}CH_2D_2$ and $\delta^{13}C$ for the same samples. The curve on the right-hand panel is a mixing model between the two extreme compositions. The shaded panel is to enhance the perspective view for the mixing curve.

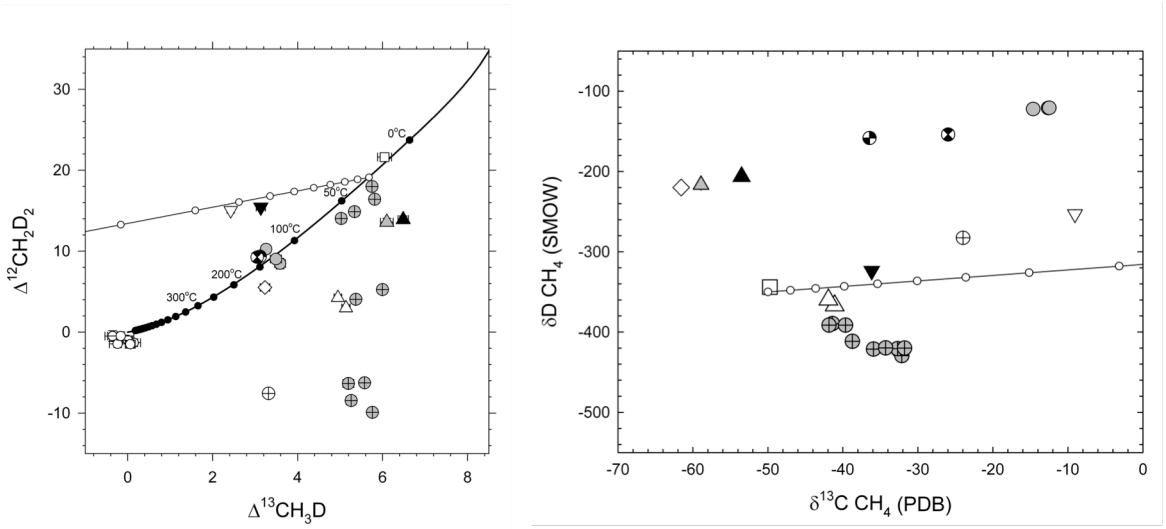

Figure 17. Plots showing the calculated compositions of methane gas residues following Rayleigh fractionation by molecular diffusion. The residue compositions are shown as the thin solid lines with white small circles in $\Delta^{12}CH_2D_2$ vs. $\Delta^{13}CH_3D$ space (left) and in δD vs. $\delta^{13}C$ space (right). Small white circles are fractions of CH_4 gas remaining in 10% increments, starting with 100%. The initial gas is on the equilibrium curve in $\Delta^{12}CH_2D_2$ vs. $\Delta^{13}CH_3D$ space (thick black curve, left panel) at 30°C. Sample symbols are the same as in the previous figures.

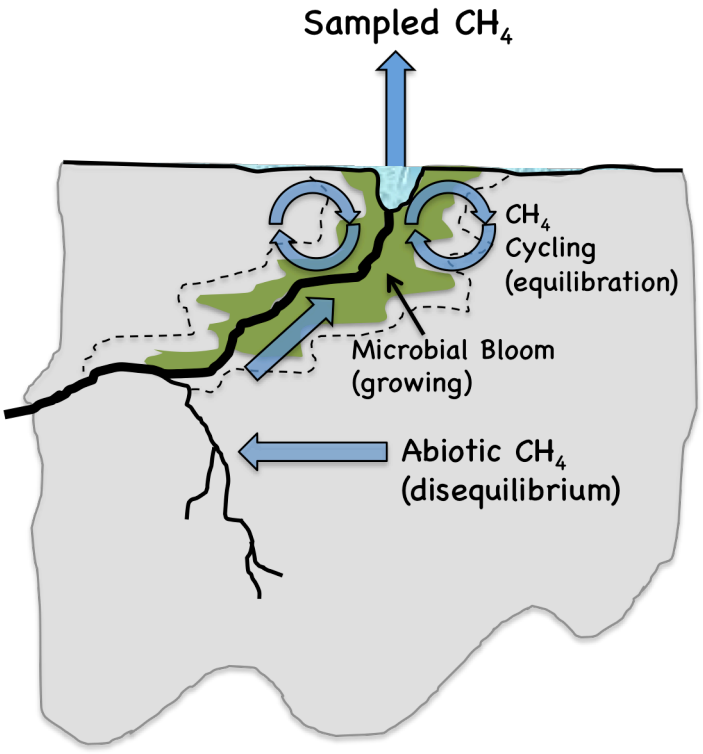

Figure 18. Schematic illustrating the scenario for abiotic methane production followed by recycling of methane by microbial activity at Kidd Creek and other deep mines. Heavy black lines represent fractures. The green field and the dashed curve represent the extent of current and future microbial communities, respectively. The blue arrows depict the path of methane gas through the fracture system, including cycling by microbial activity near the drill hole (drill hole shown at the top of the diagram).